



THE UNIVERSITY *of* EDINBURGH

Edinburgh Research Explorer

On the Role of Stern and Diffuse Layer Polarization Mechanisms in Porous Media

Citation for published version:

Bücker, M, Flores Orozco, A, Undorf, S & Kemna, A 2019, 'On the Role of Stern and Diffuse Layer Polarization Mechanisms in Porous Media' *Journal of Geophysical Research: Solid Earth*. DOI: 10.1029/2019JB017679

Digital Object Identifier (DOI):

[10.1029/2019JB017679](https://doi.org/10.1029/2019JB017679)

Link:

[Link to publication record in Edinburgh Research Explorer](#)

Document Version:

Peer reviewed version

Published In:

Journal of Geophysical Research: Solid Earth

General rights

Copyright for the publications made accessible via the Edinburgh Research Explorer is retained by the author(s) and / or other copyright owners and it is a condition of accessing these publications that users recognise and abide by the legal requirements associated with these rights.

Take down policy

The University of Edinburgh has made every reasonable effort to ensure that Edinburgh Research Explorer content complies with UK legislation. If you believe that the public display of this file breaches copyright please contact openaccess@ed.ac.uk providing details, and we will remove access to the work immediately and investigate your claim.



On the Role of Stern- and Diffuse-Layer Polarization Mechanisms in Porous Media

Matthias Buecker^{1,2,3}, Adrián Flores Orozco²,
Sabine Undorf^{3,4}, Andreas Kemna³

¹TU Braunschweig, Institute for Geophysics and extraterrestrial Physics, Mendelssohnstraße 3, 38106 Braunschweig, Germany.

²TU-Wien, Department of Geodesy and Geoinformation, Research Group Geophysics, Gußhausstraße 27-29/E120, 1040 Vienna, Austria.

³Rheinische Friedrich-Wilhelms-Universität Bonn, Institute of Geosciences, Geophysics Section, Meckenheimer Allee 176, 53115 Bonn, Germany.

⁴University of Edinburgh, School of GeoSciences, Crew Building, The King's Buildings, Alexander Crum Brown Road, Edinburgh EH9 3FF, United Kingdom.

Key Points:

- We investigate Maxwell-Wagner, Stern-layer, diffuse-layer, and membrane polarization in porous media in a generalized mathematical framework.
- Numerical and analytical solutions are mutually verified and existing analytical models of the four mechanisms are improved.
- Low-frequency Stern-layer polarization is stronger than diffuse-layer polarization if the electrical double layer is discontinuous, only.

This article has been accepted for publication and undergone full peer review but has not been through the copyediting, typesetting, pagination and proofreading process which may lead to differences between this version and the Version of Record. Please cite this article as doi: 10.1029/2019JB017679

Corresponding author: Matthias Buecker, m.buecker@tu-bs.de

Abstract

Water-saturated porous media exhibit a low-frequency (< 1 MHz) dispersion of the electrical conductivity caused by the polarization of the electrical double layer (EDL) coating the charged solid-liquid interface. We develop a mathematical framework describing the polarization caused by field-induced perturbations of the ion densities in the Stern and the diffuse layer of the EDL for two different geometrical configurations of solid and liquid phase. For spherical grains immersed in an electrolyte we derive an improved analytical description by combining suitable models for diffuse- and Stern-layer polarization. The selected models differ from those usually used in geophysical literature and improve the agreement with the corresponding finite-element (FE) solution significantly. We then employ the validated FE model to examine the EDL in a pore-constriction geometry, which is often used to study membrane polarization. Here, a suitable analytical model can only be set up for a pure diffuse-layer polarization. The results for the coupled Stern- and diffuse-layer polarization in both geometries indicate that (1) the polarization of the Stern layer is much stronger than the polarization of the diffuse layer as long as the EDL is not connected at the system scale; (2) this dominance of the Stern-layer polarization can be observed in both geometries, but (3) the contribution of the diffuse layer increases with increasing compaction as represented by the pore-constriction geometry; and (4) the contributions of both parts of the EDL reach similar levels, when the EDLs on different surfaces are interconnected at the system scale.

1 Introduction

Complex-conductivity measurements assess the frequency-dependent electrical conduction and polarization properties of soil and subsurface materials. Because macroscopic measurements are correlated to pore and/or grain geometry, electrochemical characteristics of the solid-liquid interface, and of the pore-filling electrolyte, the method has a huge potential for novel hydrogeophysical (e.g., Börner et al., 1996; Hördt et al., 2009) and biogeophysical (e.g., Atekwana & Slater, 2009; Flores Orozco et al., 2011; Wainwright et al., 2015) applications. Although empirical relations based on these correlations are increasingly used in near-surface studies, there is no widely accepted model linking macroscopic polarization effects to microscopic properties (e.g., Kemna et al., 2012). In absence of conductive minerals, four mechanisms contribute to the low-frequency (< 1 MHz) dispersion of complex conductivity, all of which are sensitive to the polarization of dif-

52 ferent parts of the electrical double layer (EDL) at the solid-liquid interface (e.g., Lesmes
53 & Morgan, 2001): (1) Maxwell-Wagner polarization, (2) polarization of the Stern layer,
54 (3) polarization of the diffuse layer, and (4) membrane polarization.

55 Maxwell (1892) and Wagner (1914) studied interfacial polarization in heterogeneous
56 media consisting of two or more phases of different electrical conductivity and/or dielec-
57 tric constant: unequal conduction and displacement current densities in the different phases
58 are balanced by an accumulation of charge along the geometrical boundaries. O’Konski
59 (1960) extended the Maxwell-Wagner theory to include the polarization of charges bound
60 to the surface of charged particles. Later, Garcia et al. (1985) treated the case of uncharged
61 dielectric particles in electrolyte solution. In contrast to earlier theories, which assume
62 homogeneous conductivities in both phases resulting in true surface charge distributions,
63 their treatment accounts for local field-induced concentration variations in the electrolyte
64 and thus volume charge of finite extension. The characteristic time scales of the differ-
65 ent types of Maxwell-Wagner polarization are short, such that this relaxation usually oc-
66 curs at the high-frequency limit (kHz) of the complex-conductivity response (e.g., Leroy
67 et al., 2008; Lesmes & Morgan, 2001).

68 A first theory describing the polarization of the Stern layer was presented by Schwarz
69 (1962) and improved by Schurr (1964). Schwarz’ theory accounts for the diffusion-controlled
70 polarization of the Stern layer of bound counter-ions. Schurr combined this model with
71 the one by O’Konski to include the effect of surface conductivity due to the diffuse layer.
72 Because the contribution of the diffuse layer is frequency independent in this model, the
73 dispersion of the complex conductivity is attributed to Stern-layer polarization and the
74 diffuse layer only results in a uniform increase of the real part of the conductivity. Later,
75 Schurr’s model provided the basis for the treatment by Leroy et al. (2008), which includes
76 a detailed electro-chemical model to quantify the partition of charges into Stern and dif-
77 fuse layer (see e.g., Revil & Glover, 1997, 1998) and also accounts for a grain-size dis-
78 tribution. This model successfully predicted the response of glass beads (Leroy et al.,
79 2008) and was extended to sand-oil-water mixtures later (Schmutz et al., 2010).

80 The polarization of the diffuse layer has been studied by Dukhin and Shilov (1974),
81 who developed a theory for the ion fluxes through thin diffuse layers, which induce con-
82 centration variations in the diffuse layer and the adjacent electrolyte. This concentration-
83 polarization mechanism has also been treated analytically by Fixman (1980), Chew and

84 Sen (1982a), and Hinch et al. (1984) among others. A numerical solution removing many
85 of the limitations of the analytical approaches – e.g., the assumption of a thin diffuse layer
86 compared to the particle radius, a sufficiently small surface potential, and a monovalent
87 symmetric electrolyte – was presented by DeLacey and White (1981). Later, Shilov et
88 al. (2001) included the effect of Maxwell-Wagner polarization into the classical Dukhin-
89 Shilov theory yielding a good agreement with the numerical model by DeLacey and White
90 (1981).

91 Different attempts have been made to determine the relative importance of Stern-
92 and diffuse-layer polarization and to develop combined models. Lyklema et al. (1983)
93 generalized the Schwarz-Schurr model by including the coupling of charges in the Stern
94 layer to those in the diffuse layer, which mainly results in a decrease of the relaxation
95 time scale. Leroy et al. (2017) applied this approach to model the polarization response
96 of calcite precipitations on glass beads. de Lima and Sharma (1992) analysed the mod-
97 els by Schwarz, Schurr, and Fixman separately in order to assess their relative contri-
98 bution to the overall polarization response. By superposing the individual responses, Lesmes
99 and Morgan (2001) developed a combined model considering all three polarization mech-
100 anisms, i.e., Stern-/diffuse-layer and Maxwell-Wagner polarization. The authors also in-
101 cluded a volume-averaging approach to study water-particle mixtures characterized by
102 a grain-size distribution. Based on the work of Kijlstra et al. (1992), Shilov et al. (2001)
103 modified the Dukhin-Shilov theory to account for the contribution of the Stern layer to
104 surface conductivity.

105 Most theories describing the first three polarization mechanism rest on the ana-
106 lytical solution of the underlying system of partial differential equations around one iso-
107 lated spherical particle. The induced dipole moment of the polarized particle obtained
108 from such treatment can then be used to derive the effective conductivity (or the effec-
109 tive dielectric constant) of ensembles of more than one particle. The effective medium
110 theory provides mixing laws for dilute suspensions (e.g., Maxwell, 1892; Wagner, 1914)
111 or mixtures with higher particle concentrations (e.g., Bruggeman, 1935; Hanai, 1960).

112 Membrane polarization is generally studied on pore networks with different levels
113 of complexity. Marshall and Madden (1959) developed the first model for a sequence of
114 two types of one-dimensional pores or zones. The membrane effect is introduced by as-
115 suming different mobilities for cations and anions in the "active" zone. While these au-

116 thors do not further specify the origin of mobility variations, later developments related
117 ion selectivity to the unequal contributions of cations and anions to the surface conduc-
118 tivity at the pore wall (Fridrikhsberg & Sidorova, 1961; Buchheim & Irmer, 1979; Titov
119 et al., 2002, 2004). Blaschek and Hördt (2009) carried out numerical simulations on one-
120 and two-dimensional pore networks, where the ion-selective behaviour of narrow pores
121 is still parameterized in terms of ion mobilities, which are constant over the pore cross
122 section. Volkmann and Klitzsch (2010) improved this approach and limited the ion se-
123 lectivity – expressed in terms of unequal effective ion mobilities – to a thin layer cover-
124 ing the pore walls.

125 Bückner and Hördt (2013a) proposed an analytical model, which allows to explic-
126 itly include pore radii and surface conductivity due to Stern and diffuse layer into the
127 one-dimensional impedance model by Marshall and Madden. This model has later been
128 extended to model the effect of temperature, fluid salinity, pH, and immiscible hydro-
129 carbon contaminants on the polarization response (Bairlein et al., 2016; Hördt et al., 2016;
130 Bückner et al., 2017). Based on the same model, Stebner and Hördt (2017) used impedance
131 networks to model the membrane polarization of porous media. Because the model by
132 Bückner and Hördt typically requires large aspect ratios, (length of a pore divided by its
133 diameter), to produce measurable polarization magnitudes, Hördt et al. (2017) further
134 investigated into the geometrical constraints of this membrane-polarization model.

135 Besides geometrical constraints, the simplified consideration of the Stern layer is
136 a major limitation of the existing theoretical treatment of membrane polarization. While
137 combined treatments of Stern-, diffuse-layer, and Maxwell-Wagner polarization mech-
138 anisms exist for grain-based models, the coupling between these three mechanisms is of-
139 ten largely simplified in pore-constriction models. Irrespective from the model geome-
140 try, the complexity of the equations for the fully coupled system describing all three mech-
141 anisms, puts a challenge on analytical solutions, which therefore all suffer from strong
142 simplifications or only treat limiting cases.

143 The present paper addresses the repeatedly stated need for "a mechanistic approach
144 and [...] general framework in which all these mechanisms are explained and quantified
145 in their relative importance" (Kemna et al., 2012). In the theory section, we compile the
146 mathematical descriptions of all relevant physical processes and provide a mathemat-
147 ical framework, which allows modelling the fully-coupled interplay of Stern- and diffuse-

148 layer polarization on arbitrary geometries. Subsequently, we derive an improved analyt-
149 ical approximation for the polarization of a single grain, which matches the results ob-
150 tained from numerically solving the equations of the generalized mathematical frame-
151 work. The validated numerical model is then applied to the pore-constriction geometry.
152 Based on the comparison of numerical and analytical results, we improve the membrane-
153 polarization model by Bückner and Hördt (2013a) and for the first time study the fully
154 coupled Stern- and diffuse-layer polarization in a pore-constriction geometry.

55 2 Theory

156 2.1 Electrical Double Layer Model

157 Most solid surfaces in contact with aqueous solutions are charged. We will consider
158 silica surfaces in contact with a monovalent electrolyte, such as NaCl, where the depro-
159 tonation of silanol surface sites produces a negative surface-charge density Σ over a wide
160 pH range (e.g., Somasundaran, 2006; Leroy et al., 2008). In the electrolyte next to the
161 silica surface, the electric field of Σ attracts counter-ions (cations, if $\Sigma < 0$) and repels
162 co-ions (here anions) giving rise to the development of two layers: The inner layer – also
163 known as Stern or Helmholtz layer – consists of counter-ions adsorbed to the silica sur-
164 face. The outer layer – also known as diffuse or Gouy-Chapman layer – is mainly pop-
165 ulated by counter-ions and a minor fraction of co-ions both obeying Poisson-Boltzmann
166 statistics.

167 We adopt the simplified model displayed in Figure 1. The Stern layer is treated as
168 an infinitely thin layer of counter-ions (e.g., Schwarz, 1962; Schurr, 1964; Leroy et al.,
2008) and is characterized by the uniform surface charge density $|\Sigma_S^{(0)}| < |\Sigma|$ [the su-
170 perscript (0) indicates quantities in the equilibrium state, i.e., without external excita-
171 tion], which partly shields the electric field of Σ . Furthermore, we assume that charges
172 in the Stern layer can only move along the surface, which reflects a strong binding of counter-
173 ions to the surface.

174 The movement of the ions in the diffuse layer is not restricted to the surface, i.e.,
175 these ions can move in all directions. As a result of an equilibrium between simultane-
176 ously acting electrostatic forces and thermal fluctuations, counter-ion excess and co-ion
177 deficit concentrations smoothly decay with the distance d from the surface. At a far dis-
178 tance from the surface, both ion concentrations approach their values in the bulk elec-

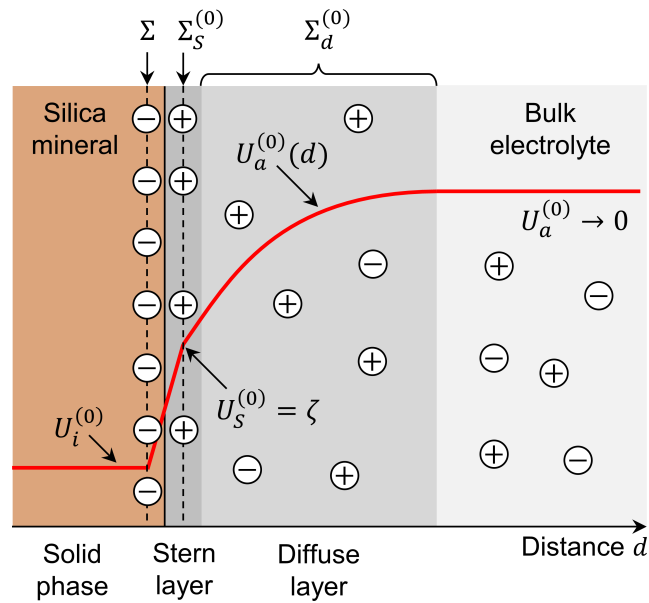


Figure 1. Simplified model of the equilibrium electrical double layer (EDL) at the charged silica surface. Due to the deprotonation of silanol surface sites, the mineral surface acquires the surface charge Σ . In the electrolyte, this usually negative charge is screened by an equal number of the positive charges distributed over the Stern layer ($\Sigma_S^{(0)}$) and the diffuse layer ($\Sigma_D^{(0)}$). The red line sketches the spatial variation of the electrical potential $U^{(0)}$ across the different parts of the EDL.

179 trolyte. Together with $\Sigma_S^{(0)}$, the total positive charge density $\rho(d)$ in the diffuse layer screens
 180 the negative surface charge Σ . By integrating $\rho(d)$ across the diffuse layer, we obtain the
 181 equivalent surface charge density $\Sigma_d^{(0)}$ of the diffuse layer. In equilibrium, the EDL con-
 182 sisting of charged surface sites, Stern layer, and diffuse layer is electro-neutral, i.e., $\Sigma_S^{(0)} +$
 183 $\Sigma_d^{(0)} = -\Sigma$.

184 The electric potential at the inner limit of the diffuse layer is usually identified with
 185 the ζ -potential at the plane of shear (e.g., Leroy et al., 2008; Bückner & Hördt, 2013a).
 186 Due to the space charge ρ , the electric potential $U_a^{(0)}$ in the electrolyte decays from ζ
 187 at the solid-liquid interface to zero in the bulk electrolyte. Note that in the simplified
 188 model sketched in Figure 1, the (equilibrium) potential in the Stern layer $U_S^{(0)}$ is equal
 189 to ζ .

190 2.2 Basic Equations

191 2.2.1 Bulk Electrolyte and Diffuse Layer

192 The bulk electrolyte is characterized by the ion valences z_{\pm} , mobilities μ_{\pm} , and bulk
 193 concentrations C_{\pm}^{∞} , as well as the relative permittivity ε_a . For the sake of simplicity, we
 194 assume that the mobilities of cations (subindex +) and anions (subindex -) are equal,
 195 i.e., $\mu_+ = \mu_- = \mu$, and limit our treatment to monovalent electrolytes, i.e., $z_{\pm} = \pm 1$.
 196 In the case of a dilute solution, the electrical conductivity of the bulk electrolyte is then
 197 given by $\sigma_a = 2e\mu C_{\pm}^{\infty}$.

198 Spatial and temporal variations of the ion concentrations $C_{\pm}(\mathbf{r}, t)$ and the electri-
 199 cal potential $U_a(\mathbf{r}, t)$ in the solution, i.e., in the diffuse layer and the bulk electrolyte,
 200 are controlled by the steady-state Nernst-Planck, mass continuity, and Poisson equations
 201 (e.g., Garcia et al., 1985):

$$202 \quad \mathbf{J}_{\pm}(\mathbf{r}, t) = -D\nabla C_{\pm}(\mathbf{r}, t) - z_{\pm}\mu C_{\pm}(\mathbf{r}, t)\nabla U_a(\mathbf{r}, t) \quad (1)$$

$$203 \quad \nabla \cdot \mathbf{J}_{\pm}(\mathbf{r}, t) = -\partial_t C_{\pm}(\mathbf{r}, t) \quad (2)$$

$$204 \quad \nabla^2 U_a(\mathbf{r}, t) = -\frac{e}{\varepsilon_0 \varepsilon_a} [C_+(\mathbf{r}, t) - C_-(\mathbf{r}, t)] \quad (3)$$

205 Here, D denotes the diffusion coefficient, $e = 1.602 \times 10^{-19}$ C is the elementary charge,
 206 and $\varepsilon_0 = 8.85 \times 10^{-12}$ F/m is the vacuum permittivity. In absence of specific interac-
 207 tion between the different ion species, the Einstein relation $D = \mu k_B T / e$ can be used
 208 to connect diffusion coefficient and mobility of the ions. Here, $k_B = 1.381 \times 10^{-23}$ J/K

is Boltzmann's constant and T is the absolute temperature. The current densities \mathbf{J}_{\pm} defined by the steady-state Nernst-Planck equation 1 consider diffusion $-D\nabla C_{\pm}$ and electro-migration $-z_{\pm}\mu C_{\pm}\nabla U_a$ ion fluxes.

If the system is excited by a time-harmonic electric field $E_0 e^{i\omega t}$, where ω and t denote angular frequency and time, respectively, the ion concentrations $C_{\pm}(\mathbf{r}, t)$ can be expressed by the sums of the static equilibrium concentrations $C_{\pm}^{(0)}$ and perturbation concentrations $|\delta C_{\pm}|$ (e.g., Garcia et al., 1985):

$$C_{\pm}(\mathbf{r}, t) = C_{\pm}^{(0)}(\mathbf{r}) + \delta C_{\pm}(\mathbf{r}, \omega) \cdot e^{i\omega t} \quad (4)$$

The electrical potential $U_a(\mathbf{r}, t)$ can also be decomposed into the static equilibrium potential $U_a^{(0)}$ and the perturbation $|\delta U_a| \ll U_a^{(0)}$:

$$U_a(\mathbf{r}, t) = U_a^{(0)}(\mathbf{r}) + \delta U_a(\mathbf{r}, \omega) \cdot e^{i\omega t} \quad (5)$$

By inserting equations 4 and 5 into equations 1 through 3 and Fourier-transforming the resulting system, the problem can be decomposed into a static part and a frequency-dependent part (e.g., Chew & Sen, 1982b, 1982a). While the frequency-dependent part couples to the static solution, the static part can be solved independently.

To obtain the static part of the system, we set $\delta C_{\pm}, \delta U_a, \partial_t = 0$. After a few additional manipulations, this yields the Boltzmann-distributed equilibrium ion concentrations (Chew & Sen, 1982b)

$$C_{\pm}^{(0)}(\mathbf{r}) = C_{\pm}^{\infty} \exp \left[-\frac{z_{\pm} e}{k_B T} U_a^{(0)}(\mathbf{r}) \right] \quad (6)$$

and the Poisson-Boltzmann equation (e.g., Chew & Sen, 1982b)

$$\nabla^2 U_a^{(0)}(\mathbf{r}) = -\kappa^2 \frac{k_B T}{e} \sinh \left[\frac{e}{k_B T} U_a^{(0)}(\mathbf{r}) \right], \quad (7)$$

where $\kappa = [2e^2 C_{\pm}^{\infty} / (\varepsilon_0 \varepsilon_f k_B T)]^{1/2}$ is the inverse Debye screening length. Together with the boundary conditions discussed below, equations 6 and 7 describe the equilibrium ion concentrations C_{\pm}^{∞} and the static electrical potential $U_a^{(0)}$ in the diffuse layer and the bulk electrolyte.

In order to obtain the solution of the frequency-dependent system under the influence of a weak external field $E_0 \exp(i\omega t)$, the steady-state Nernst-Planck equation 1 is inserted into the continuity equation 2, Fourier-transformed and linearized, which gives

237 (e.g., Chew & Sen, 1982a)

$$238 \quad i\omega\delta C_{\pm}(\mathbf{r}, \omega) = \nabla \left\{ D\nabla\delta C_{\pm}(\mathbf{r}, \omega) \right. \\ 239 \quad \left. + \mu z_{\pm} \left[C_{\pm}^{(0)}(\mathbf{r})\nabla\delta U_a(\mathbf{r}, \omega) + \delta C_{\pm}(\mathbf{r}, \omega)\nabla U_a^{(0)}(\mathbf{r}) \right] \right\} + \mathcal{O}(E_0^2). \quad (8)$$

240 The frequency-dependent perturbation concentrations of the two ion species and the po-
241 tentials are coupled to each other by the Fourier-transformed Poisson equation (e.g., Chew
242 & Sen, 1982a)

$$243 \quad \nabla^2\delta U_a(\mathbf{r}, \omega) = -\frac{e}{\varepsilon_0\varepsilon_r} [\delta C_+(\mathbf{r}, \omega) - \delta C_-(\mathbf{r}, \omega)]. \quad (9)$$

244 Equations 8 and 9 constitute three coupled partial differential equations that describe
245 the spatial variations of the perturbation quantities. As the boundary conditions at the
246 solid surface link the solution in the electrolyte to the corresponding solutions in the Stern
247 layer and the interior of the solid, we will discuss the boundary conditions further be-
248 low.

249 **2.2.2 Stern Layer**

250 The Stern layer is modelled as a thin layer situated at the solid-liquid interface. In
251 absence of an external excitation, the surface-charge density $\Sigma_S^{(0)}$ in this layer is uniform.
252 Under the influence of the electrical field $E_0 \exp(i\omega t)$, the counter-ions move along the
253 surface, but no charge exchange with the electrolyte nor the solid is considered. We de-
254 scribe the surface-charge density in the Stern layer in terms of the constant equilibrium
255 value $\Sigma_S^{(0)}$ and the perturbation $|\delta\Sigma_S| \ll \Sigma_S^{(0)}$, such that

$$256 \quad \Sigma_S(\mathbf{r}_S, t) = \Sigma_S^{(0)} + \delta\Sigma_S(\mathbf{r}_S, \omega) \exp(i\omega t), \quad (10)$$

257 where \mathbf{r}_S denotes the position vector in local coordinates along the solid-liquid interface.
258 Adopting the treatment of the bound surface-charge densities on spherical particles pro-
259 posed by Schwarz (1962) and Schurr (1964), the perturbation of the surface-charge den-
260 sity in the Stern layer is controlled by

$$261 \quad i\omega\delta\Sigma_S(\mathbf{r}_S, \omega) = \nabla_S \left[D_S\nabla_S\delta\Sigma_S(\mathbf{r}_S, \omega) + \mu_S\Sigma_S^{(0)}\nabla_S\delta U_S(\mathbf{r}_S, \omega) \right] + \mathcal{O}(E_0^2), \quad (11)$$

262 where ∇_S is the surface Laplacian operating on functions defined on the geometrical bound-
263 ary (also known as Laplace-Beltrami operator), μ_S is the mobility, D_S is the diffusion
264 coefficient, and δU_S is the perturbation potential in the Stern layer. Note that equation

11 is the surface equivalent of equation 8 describing diffusion and electro-migration surface-flux densities within the Stern layer. Only the third term on the right hand side of equation 8 has no equivalent because the constant potential results in a vanishing tangential electrical field $-\nabla_S U_S^{(0)}$.

For spherical particles of radius a centered at the origin of the spherical coordinate system (r, θ, ϕ) and an excitation parallel to the polar axis $\theta = 0$, equation 11 takes the form (e.g., Schurr, 1964; Schwarz, 1962)

$$i\omega\delta\Sigma_S(\theta, \omega) = \frac{1}{a^2 \sin\theta} \frac{\partial}{\partial\theta} \left[D_S \sin\theta \frac{\partial}{\partial\theta} \delta\Sigma_S(\theta, \omega) + \mu_S \Sigma_S^{(0)} \sin\theta \frac{\partial}{\partial\theta} \delta U_S(\theta, \omega) \right]. \quad (12)$$

There is no particular surface equivalent of Poisson's equation 9. Instead, the continuity of the electrical potential at the solid surface (in conjunction with the vanishing thickness of the Stern layer) directly couples δU_S and the surface-charge density $\delta\Sigma_S$ to the adjacent perturbation potentials in electrolyte and solid.

2.2.3 Solid Dielectric

The solid dielectric has a relative permittivity ε_i and zero electrical conductivity. The spatial variation of the potential within the solid is governed by the Laplace equation $\nabla^2 U_i(\mathbf{r}, t) = 0$. In equilibrium, the static electrical potential $U_i^{(0)}$ must be equal to the (constant) ζ -potential on the surface and $U_i^{(0)}$ must be constant throughout the solid. The Fourier-transformed frequency-dependent Laplace equation writes

$$\nabla^2 \delta U_i(\mathbf{r}, \omega) = 0, \quad (13)$$

which in conjunction with the spatially varying surface potential $\delta U_S(\mathbf{r}_S, \omega)$ determines the perturbation potential $\delta U_i(\mathbf{r}, \omega)$ within the solid.

2.3 Boundary Conditions

At far distances d from the surface, the static background potential in the electrolyte should approach zero, i.e.,

$$U_a^{(0)} \xrightarrow{d \rightarrow \infty} 0. \quad (14)$$

At the surface, we take advantage of our knowledge of the constant potential $U_i^{(0)}$ inside of the solid (see above) and use the continuity of the displacement current to de-

292 fine the Neumann boundary condition

$$293 \quad -\varepsilon_0 \varepsilon_a \nabla U_a^{(0)} \Big|_{\text{surface}} \cdot \mathbf{n} = \Sigma + \Sigma_S^{(0)}, \quad (15)$$

294 where \mathbf{n} denotes the unit normal vector to the solid surface (pointing out of the solid into
295 the electrolyte) and $\Sigma + \Sigma_S^{(0)} = -\Sigma_d^{(0)}$ is the net surface-charge density. The bound-
296 ary conditions on the equilibrium ion concentrations $C_{\pm}^{(0)}$ are implicit to equation 6.

297 The perturbation potential at far distances d from the surface must be equal to val-
298 ues corresponding to the external electrical field, i.e.,

$$299 \quad \delta U_a(\mathbf{r}, \omega) \xrightarrow{d \rightarrow \infty} -\mathbf{E}_{\text{ext}}(\mathbf{r}) \cdot \mathbf{r}, \quad (16)$$

300 while the ion concentrations should approach their bulk values, i.e.,

$$301 \quad \delta C_{\pm}(\mathbf{r}, \omega) \xrightarrow{d \rightarrow \infty} 0. \quad (17)$$

302 At the surface of the solid, the solutions for the three model domains – electrolyte, Stern
303 layer, and solid – are pieced together. The continuity of the electrical potential demands
304 the three perturbation potentials to be equal at any point \mathbf{r}_S on the surface, i.e.,

$$305 \quad \delta U_i(\mathbf{r}_S, \omega) = \delta U_S(\mathbf{r}_S, \omega) = \delta U_a(\mathbf{r}_S, \omega). \quad (18)$$

306 We assume that on the time scales of interest, ions of the solution do not engage in sur-
307 face reactions, thus they are neither produced nor consumed and the normal fluxes through
308 the surface are zero, i.e.,

$$309 \quad \left\{ -D \nabla \delta C_{\pm}(\mathbf{r}, \omega) - \mu z_{\pm} \left[C_{\pm}^{(0)}(\mathbf{r}, \omega) \nabla \delta U_a(\mathbf{r}, \omega) + \delta C_{\pm}(\mathbf{r}, \omega) \nabla U_a^{(0)}(\mathbf{r}, \omega) \right] \right\} \Big|_{\mathbf{r}=\mathbf{r}_S} \cdot \mathbf{n} = 0. \quad (19)$$

310 The continuity of the displacement current implies that (e.g., Schwarz, 1962)

$$311 \quad [-\varepsilon_0 \varepsilon_a \nabla \delta U_a(\mathbf{r}, \omega) + \varepsilon_0 \varepsilon_i \nabla \delta U_i(\mathbf{r}, \omega)] \Big|_{\mathbf{r}=\mathbf{r}_S} \cdot \mathbf{n} = \delta \Sigma_S(\mathbf{r}_S), \quad (20)$$

312 which completes the set of boundary conditions.

313 **3 Polarization of Spherical Grains**

314 The model set up in the previous section describes the charge polarization of the
315 Stern layer and the concentration polarization produced by unequal contributions of an-
316 ions and cations to electrical conduction through the diffuse layer. In this section, we
317 will study the relative importance of both polarization mechanisms for the case of di-
318 lute suspensions of dielectric spheres. Because even for spherical particles no analytical

319 solution of the fully coupled problem is known, we first obtain a suitable analytical ap-
 320 proximation of the coupled polarization process, which combines (i) the Stern-layer po-
 321 larization model by Schwarz (1962), including the correction of the corresponding relax-
 322 ation time proposed by Lyklema et al. (1983), and (ii) the diffuse-layer polarization model
 323 developed by Dukhin and Shilov (1974). In order to assess the quality of our analyti-
 324 cal model and open the possibility to model the polarization response of more complex
 325 geometrical configurations, we also present a numerical finite-element solution.

3.1 Analytical Model

326
 327 At distances far from a spherical particle of radius a centred at the origin of the
 328 spherical coordinate system $\mathbf{r} = (r, \theta, \phi)$, all approximate analytical solutions take the
 329 form (e.g., Maxwell, 1892; Wagner, 1914; Schurr, 1964; Dukhin & Shilov, 1974)

$$330 \quad \delta U_a(\mathbf{r}, \omega) = E_0 \left[-r + \frac{f(\omega)a^3}{r^2} \right] \cos \theta, \quad (21)$$

331 if the external excitation is parallel to the polar axis, i.e., $\theta = 0$. The first term of this
 332 expression accounts for the potential due to the external field and the second term de-
 333 scribes the effective long-range dipole moment of the polarized particle. The reflection
 334 coefficient $f(\omega)$ contains the complete information on the macroscopic polarization re-
 335 sponse of the particle. For a pure Maxwell-Wagner polarization, it writes

$$336 \quad f(\omega) = \frac{\sigma_i^*(\omega) - \sigma_a^*(\omega)}{2\sigma_a^*(\omega) + \sigma_i^*(\omega)}, \quad (22)$$

337 where $\sigma_a^*(\omega) = \sigma_a + i\omega\varepsilon_0\varepsilon_a$ and $\sigma_i^*(\omega) = i\omega\varepsilon_0\varepsilon_i$ are the complex conductivity of the
 338 bulk electrolyte and the non-conducting particle, respectively.

339 With $f(\omega)$ for one spherical particle at hand, the effective complex conductivity
 340 $\sigma^*(\omega)$ of a dilute suspension of a number of equal particles can be obtained using a gen-
 341 eralized form of the theory by Wagner (1914)

$$342 \quad \frac{\sigma^*(\omega)}{\sigma_a^*} = \frac{1 + 2\nu f(\omega)}{1 - \nu f(\omega)}, \quad (23)$$

343 where ν denotes the volume fraction of suspended particles. Together with the complex
 344 conductivities σ_a^* and σ_i^* , equations 22 and 23 describe the Maxwell-Wagner polariza-
 345 tion of suspensions of dielectric particles in a medium with homogeneous complex con-
 346 ductivity $\sigma_a^*(\omega)$.

347 O'Konski (1960) included the effect of a uniform surface charge density Σ_x into
 348 this model. He found that the effect of charge carriers that move freely along the par-

349 ticle surface can be taken into account by adding the effective conductivity increment
 350 $\sigma_x = 2\mu_x \Sigma_x / a$ to the complex conductivity σ_i^* of the particle. According to this idea,
 351 the effective conductivity of the diffuse layer can be expressed as

$$352 \quad \sigma_d = |\sigma_{d+} + \sigma_{d-}| = \frac{2\mu |\Sigma_{d+}^{(0)} - \Sigma_{d-}^{(0)}|}{a}, \quad (24)$$

353 where the contributions of the two types of ions to the effective conductivity of the dif-
 354 fuse layer are defined as

$$355 \quad \sigma_{d\pm} = \frac{\pm 2\mu \Sigma_{d\pm}^{(0)}}{a}. \quad (25)$$

356 For sufficiently thin diffuse layers, i.e., $\kappa a \ll 1$, the equivalent surface charge densities
 357 in the diffuse layer can be related to the surface charge using a variation of Bikerman's
 358 equation for the surface conductivity near a (highly) charged plane surface (e.g., Shilov
 359 et al., 2001)

$$360 \quad \Sigma_{d\pm}^{(0)} = \pm \frac{2eC_{\pm}^{\infty}}{\kappa} \left[\exp\left(\mp \frac{e\zeta}{2k_B T}\right) - 1 \right]. \quad (26)$$

361 Note that while the total charge stored in the diffuse layer is represented by the sum of
 362 both contributions, i.e., $\Sigma_d^{(0)} = \Sigma_{d+}^{(0)} + \Sigma_{d-}^{(0)}$, the total surface conductivity of the dif-
 363 fuse layer σ_d is proportional to their difference. For a given surface charge density $\Sigma_d^{(0)}$,
 364 the ζ -potential can be obtained from

$$365 \quad \zeta(\Sigma_d^{(0)}) = -\frac{2k_B T}{e} \sinh^{-1} \left(\Sigma_d^{(0)} \frac{\kappa}{4eC_{\pm}^{\infty}} \right). \quad (27)$$

366 This relation can readily be obtained from equation 26. Resolved for $\Sigma_d^{(0)}(\zeta)$, it is also
 367 known as Grahame equation (Grahame, 1947).

368 The surface-charge density of the Stern layer can be expressed in terms of the ef-
 369 fective conductivity

$$370 \quad \sigma_S = \frac{2\mu_S |\Sigma_S^{(0)}|}{a}. \quad (28)$$

371 In the present study, the partition of counter-ions into diffuse layer and Stern layer will
 372 be expressed in terms of the ratio $p = -\Sigma_S^{(0)} / \Sigma$. Note that this definition is slightly dif-
 373 ferent from the partition coefficient $f_Q = \Sigma_S^{(0)} / (\Sigma_{d+}^{(0)} + \Sigma_S^{(0)})$ introduced by Leroy and
 374 Revil (2004).

375 **3.1.1 Stern-Layer Polarization**

376 If the entire counter charge is located in the Stern layer (i.e., $p = 1$), and no dif-
 377 fuse layer is present (i.e., $\Sigma_d^{(0)}, \zeta = 0$), the low-frequency response of the particle is caused

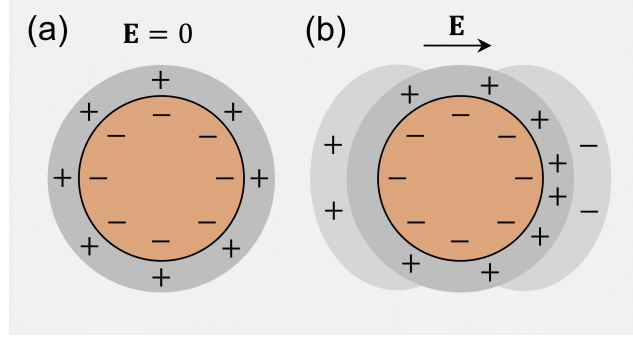


Figure 2. Sketch of the polarization of the Stern layer: (a) negatively charged particle and Stern layer in equilibrium; (b) under the influence of the external field \mathbf{E} , cations in the Stern layer move along the surface, deplete on the left side and accumulate on the right side of the particle. The resulting net surface charge $\delta\Sigma_S$ causes field-induced diffuse layers of opposite charge to build up in the electrolyte next to the charged surfaces (e.g., Lyklema et al., 1983).

378 by the polarization of the Stern layer only (see Figure 2). In the thin double layer limit,
 379 i.e., $\kappa a \ll 1$, the solution of the polarization problem can be approximated as done by
 380 Schwarz (1962). In terms of the reflection coefficient f defined in equation 21, the final
 381 result obtained by Schwarz (1962) can be expressed as (from his equation 13)

$$382 \quad f_S(\omega) = \frac{\sigma_S^*(\omega) - \sigma_a^*(\omega)}{2\sigma_a^*(\omega) + \sigma_S^*(\omega)}, \quad (29)$$

383 where σ_S^* is the effective complex conductivity of the spherical particle, which writes (from
 384 Schwarz, 1962, eq. 14 and 16)

$$385 \quad \sigma_S^*(\omega) = \sigma_S \frac{i\omega\tau_S}{1 + i\omega\tau_S} + i\omega\varepsilon_0\varepsilon_i. \quad (30)$$

386 Note that the particle is assumed to be non-conducting, i.e., $\sigma_i = 0$. The relaxation time
 387 of the Stern-layer polarization τ_S can be expressed as (Lyklema et al., 1983, eq. 36)

$$388 \quad \tau_S = \frac{a^2}{2D_S M}, \quad (31)$$

389 where the coefficient M defined as (Lyklema et al., 1983, eq. 34)

$$390 \quad M = 1 + \frac{\kappa\Sigma_S^{(0)}}{2eC_{\pm}^{\infty} \cosh[\zeta/(2k_B T)]} \quad (32)$$

391 accounts for the coupling of the charges in the Stern layer to the electrolyte, which had
 392 not been considered in the original model by Schwarz (1962).

393 Because $\zeta = 0$ if $p = 1$, there is no equilibrium diffuse layer and the polariza-
 394 tion response is only due to the polarization of the Stern layer, first term in equation 30,

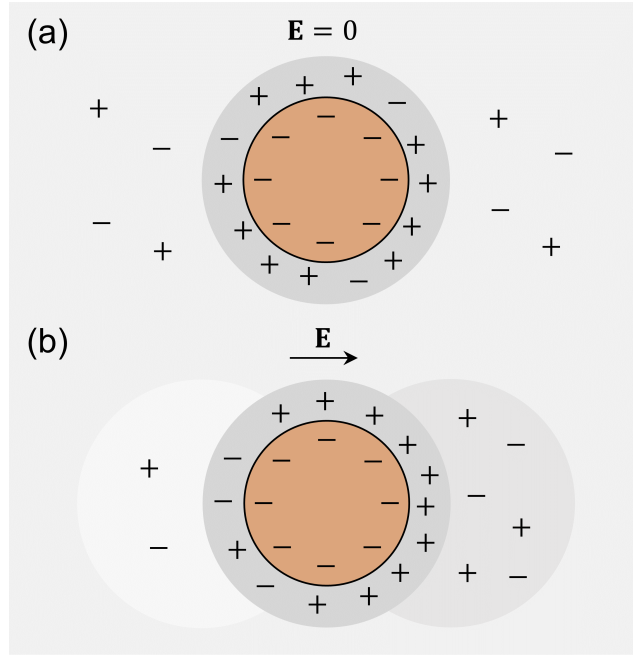


Figure 3. Sketch of the polarization of the diffuse layer: (a) negatively charged particle, diffuse layer, and bulk electrolyte in equilibrium; (b) under the influence of the external field \mathbf{E} , the high effective conductivity of the diffuse layer leads to an accumulation of positive charge on the right side and negative charge on the left side of the particle. In addition, unequal migration flux densities of cations and anions through the diffuse layer are counter-balanced by an electroneutral salinity gradient that builds up next to the particle.

and the Maxwell-Wagner polarization caused by the conductivity and permittivity contrasts between particle and electrolyte.

3.1.2 Diffuse-Layer Polarization

In the opposite case, in which no Stern layer exists (i.e., $p = 0$) and the entire counter charge is located in the diffuse layer, only the diffuse layer polarizes (see Figure 3). This scenario has been treated by Dukhin and Shilov (1974) for the limit of thin diffuse layers. If electro-osmotic effects are neglected, i.e., in the limit of an infinitely large fluid viscosity, the result of the classical Dukhin-Shilov theory can be expressed in terms of the reflection coefficient (e.g., Grosse & Shilov, 1996; Shilov et al., 2001)

$$f_d(\omega) = \frac{2Du(\zeta) - 1}{2Du(\zeta) + 2} - \frac{3S}{2} \frac{(\sigma_{d+} - \sigma_{d-})^2}{\sigma_a^2 [2Du(\zeta) + 2]^2} \left[1 - \frac{i\omega\tau_\alpha}{1 + \sqrt{i\omega 2\tau_\alpha/S} + i\omega\tau_\alpha} \right], \quad (33)$$

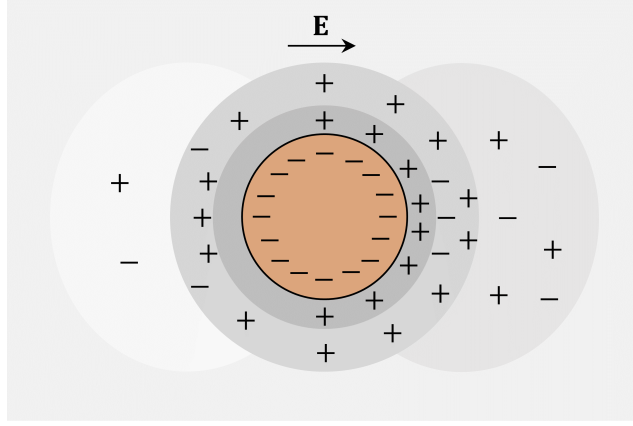


Figure 4. Sketch of the coupled polarization of Stern and diffuse layer: due to the presence of a diffuse layer, the net surface density in the polarized Stern layer $\delta\Sigma_S$ is larger than in the case without diffuse layer (Lyklema et al., 1983). In the inner part of the diffuse layer, $\delta\Sigma_S$ attracts opposite charges (here positive on the right and negative on the left side of the particle). In the outer part, the charge in the diffuse layer changes its sign, which compensates for the high effective conductivity of this layer (as in Figure 3). The salinity gradient in the electrolyte next to the particle is a result of the unequal migration flux densities of cations and anions through the diffuse layer.

where $Du(\zeta) = \sigma_d/(2\sigma_a)$ is the Dukhin number. The coefficient S , which appears in the expression for f_d , writes

$$S = \frac{[Du(\zeta) + 1] \sigma_a^2}{(\sigma_{d+} + \sigma_a)(\sigma_{d-} + \sigma_a)} \quad (34)$$

and the time constant is defined as $\tau_\alpha = a^2 S/(2D)$. The effective conductivity of the suspension can be obtained by substituting f by f_d in equation 23. Note that this formulation only accounts for the polarization of the diffuse layer; an extension including Maxwell-Wagner polarization can be found in Shilov et al. (2001).

3.1.3 Coupled Polarization

For any value $0 < p < 1$, the counter charges are distributed over Stern and diffuse layer, which leads to a simultaneous polarization of both parts of the EDL (see Figure 4). As argued by Lesmes and Morgan (2001), the coupled polarization can be approximated by a superposition of the individual responses, i.e., by adding the effective complex dielectric constants of the particle (or the corresponding effective complex-conductivity

increments). In order to obtain an effective conductivity increment describing the diffuse-layer polarization, we rearrange equation 22 as follows:

$$\sigma_d^*(\omega) = \sigma_a^*(\omega) \frac{1 + 2f_d(\omega)}{1 - f_d(\omega)}. \quad (35)$$

The effective conductivity σ_S^* , which accounts for Stern-layer and Maxwell-Wagner polarization, is given by equations 30 through 32 and, thus, the total effective conductivity of the particle including all three mechanisms writes

$$\sigma_c^*(\omega) = \sigma_d^*(\omega) + \sigma_S^*(\omega) = \sigma_d^*(\omega) + \sigma_S \frac{i\omega\tau_S}{1 + i\omega\tau_S} + i\omega\varepsilon_0\varepsilon_i. \quad (36)$$

Note that this expression is almost the same as the one obtained by Schurr (1964) except for the decrease of τ_S by the factor M and the substitution of σ_d by $\sigma_d^*(\omega)$, i.e., including the frequency-dependent contribution of the diffuse layer defined by equations 33 through 35.

The new coupled model described here is also similar to the one proposed by Lesmes and Morgan (2001), from which it differs with regard to (i) the relaxation time of the Stern layer τ_S , where we use the correction by Lyklema et al. (1983), (ii) the low-frequency contribution σ_S of the Stern layer (their equations 5 and 6), which we do not consider because it contradicts the assumption of a strongly bound Stern-layer; and (iii) the selection of the model describing the diffuse-layer polarization, where we use the Dukhin-Shilov theory instead of the model by Fixman (1980). Fixman's assumption that the co-ion contribution to the surface conductivity can be ignored for sufficiently high ζ -potentials does not hold for the range of ζ -potentials studied here. We found that this simplification significantly affects the real part of the complex conductivity (not shown here for brevity).

3.2 Numerical Model

Figure 5 shows the geometrical set-up used for the numerical modelling. The dielectric particle of radius a is centred at the origin of coordinates and the external electric field is imposed in x-direction, i.e., $\mathbf{E}_{\text{ext}} = E_0\mathbf{e}_x$, where \mathbf{e}_x denotes the unit vector in x-direction. Due to the cylindrical symmetry of the problem, the numerical simulation can be carried out on the two-dimensional model domain in Cartesian coordinates $\mathbf{r} = (x, y)$ marked in red in Figure 5.

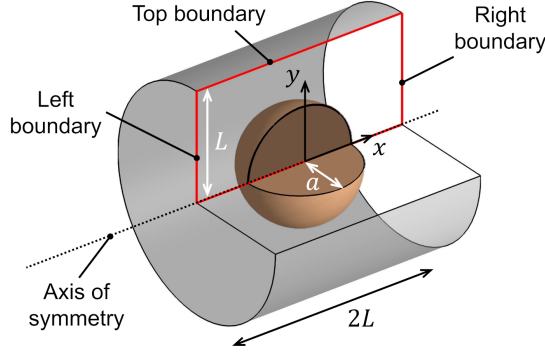


Figure 5. Three-dimensional sketch of the geometrical set-up used for the numerical simulation of the polarization around spherical particles. The particle of radius a is enclosed by a cylinder of radius L and height $2L$, which represents the electrolyte. The red rectangle marks the actual two-dimensional model domain.

47 We use the finite-element software COMSOL Multiphysics to successively obtain
 448 the static and the frequency-dependent solution. We first solve the Poisson-Boltzmann
 449 equation 7, which contains $U^{(0)}(\mathbf{r})$ as only unknown variable. For the numerical imple-
 450 mentation, boundary conditions 14 and 15 are translated as follows: $U^{(0)} = 0$ on the
 451 left, right, and top boundary; $[\varepsilon_0\varepsilon_i\nabla U_i^{(0)} - \varepsilon_0\varepsilon_a\nabla U_a^{(0)}]\mathbf{n} = -\Sigma_d^{(0)}$ on the particle sur-
 452 face; and $\partial U^{(0)}/\partial y = 0$ on the axis of symmetry. The static background ion concen-
 453 trations are computed by inserting $U_a^{(0)}$ into equation 6.

454 Subsequently, we solve the frequency-dependent part described by equations 8, 9,
 455 11, and 13 and the boundary conditions 16 through 20. For the numerical solution, the
 456 latter are adjusted as follows: $\delta n_{\pm} = 0$ and $\delta U_a = \pm E_0 L$ on the left and right bound-
 457 ary, respectively; $\mathbf{J}_{\pm} = 0$ and $\partial\delta U/\partial y = 0$ on top boundary and on the axis of sym-
 458 metry; unchanged on the particle surface. While the static solution only needs to be com-
 459 puted once for each set of model parameters (i.e., a , Σ , p , etc.), the frequency-dependent
 460 problem has to be solved for each value of the angular frequency ω separately.

461 Because bulk values are implicitly assumed on the left, right, and top boundary,
 462 these boundaries must be placed sufficiently far away from the particle surface, where
 463 the polarization is expected to cause non-zero perturbations. As a trade-off between pre-
 464 cision and computational cost, we define a standard domain size of $L = 10a$. For more
 465 technical details on the implementation, see the appendix.

The effective conductivity of the model can be obtained from the numerical integration of the total ion flux densities through the left (or likewise the right) boundary, i.e.,

$$\sigma_{\text{mod}}^* = \frac{2}{E_0 L^2} \int_0^L [\mathbf{J}_+(y) + \mathbf{J}_-(y)] \mathbf{e}_x y dy, \quad (37)$$

where the term $y dy$ accounts for the area element of the boundary and the factor $2/L^2$ stems from the normalization with the total area.

The standard domain size is $L = 10a$ and corresponds to a rather small volume fraction of dielectric particles. Therefore, we scale the modelled effective conductivities $\sigma_{\text{mod}}^*(\omega)$ to a more realistic volumetric content of $\nu = 0.4$ using the mixing rule defined in equation 23 with

$$f(\omega) = \frac{1}{\nu_{\text{mod}}} \frac{\sigma_{\text{mod}}^*(\omega) - \sigma_a^*(\omega)}{\sigma_{\text{mod}}^*(\omega) + 2\sigma_a^*(\omega)}. \quad (38)$$

3.3 Comparison of Analytical and Numerical Solution

Unless otherwise stated, the following parameter values are used to obtain both numerical and analytical results: the relative permittivities are $\varepsilon_a = 80$ for the aqueous electrolyte and $\varepsilon_i = 4.5$ for the solid, which is a typical value for quartz sand (e.g., Robinson & Friedman, 2003). The uniform ion mobility is $\mu = 5 \cdot 10^{-8} \text{ m}^2/(\text{Vs})$, which is approximately equal to the mobility of the sodium cation (e.g., Atkins & De Paula, 2013) and will be used for both ion species in the electrolyte. The mobility of the counter-ions in the Stern layer is only 10% of the ion mobility in the bulk electrolyte, i.e., $\mu_S = \mu/10$. This value corresponds to the reduction of the cation mobility in the Stern layer inferred for K^+ on latex surfaces by Zukoski and Saville (1986) and for Na^+ on clay surfaces by Revil and Glover (1998) and Revil et al. (1998). For near-neutral pH of the solution and ion concentrations in the bulk electrolyte of $C_{\pm}^{\infty} = 1 \text{ mol/m}^2$, it is adequate to assume a surface charge density of $\Sigma = -0.01 \text{ C/m}^2$ (e.g., Kosmulski, 2006). The absolute temperature of $T = 293 \text{ K}$ (room temperature) and the above-mentioned volumetric content of $\nu = 0.4$ complete the set of standard model parameters.

Figure 6 displays the conductivity spectra of a suspension of spherical particles of radius $a = 5 \mu\text{m}$ for six values of p between 0 and 1. The effective conductivity of the mixture σ^* is expressed in terms of the corresponding real (σ') and imaginary (σ'') parts. In Figure 6a, we observe a continuous decrease of σ' with increasing p . This means that the surface conductivity due to counter-ions in the diffuse layer is much larger than the

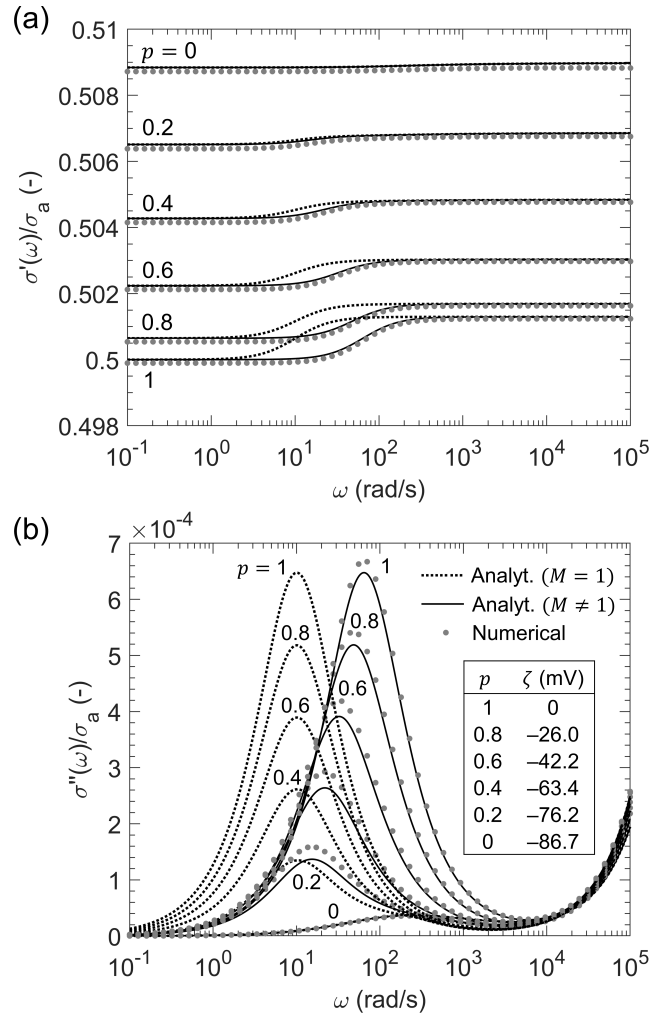


Figure 6. Complex-conductivity spectra of a suspension of dielectric particles of radius $a = 5 \mu\text{m}$ at different ratios $p = -\Sigma_S^{(0)}/\Sigma$, i.e., the surface charge in the Stern layer increases with p . Complex-valued conductivities in terms of real (a) and imaginary (b) parts normalized to the bulk conductivity σ_a . Numerical results (grey circles) are displayed along with the corresponding analytical models according to equation 36 using the simple relaxation time after Schwarz (1962) ($M = 1$ in equation 31, dotted line) and using the corrected relaxation time after Lyklema et al. (1983) ($M \neq 1$, solid line). The values of ζ shown in (b) are computed from equation 27.

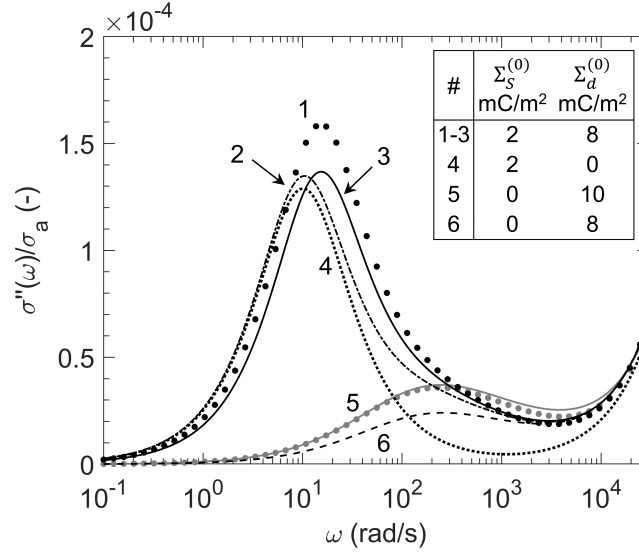


Figure 7. Numerical (filled circles) and analytical (lines) imaginary conductivity spectra for small surface charge densities $\Sigma_S^{(0)}$ in the Stern layer. Analytical curves are calculated from equation 36, using the values of $\Sigma_S^{(0)}$ and $\Sigma_d^{(0)}$ given in this Figure. Curve 1: numerical solution for the coupled Stern and diffuse-layer polarization; curves 2 and 3: analytical solution for the coupled Stern and diffuse-layer polarization using $M = 1$ and $M \neq 1$ in equation 31, respectively; curve 4: analytical solution for a pure Stern-layer polarization using $M = 1$; curves 5 and 6: numerical and analytical solutions for a pure diffuse-layer polarization and two different surface charge densities $\Sigma_d^{(0)}$ in the diffuse layer.

497 one of the Stern layer. This is due, on the one hand, to the significantly reduced mobil-
 498 ity of the counter-ions in the Stern layer, which affects all frequencies equally. On the
 499 other hand, at low frequencies, the Stern layer is completely polarized and does not con-
 500 tribute to the DC conductivity because we assume that it cannot exchange ions with the
 501 bulk electrolyte. However, the Stern layer does contribute to the high-frequency limit
 502 of σ' , i.e., at frequencies larger than the characteristic frequency of the Stern-layer po-
 503 larization. The higher p and thus the surface conductivity σ_S , the larger becomes the
 504 difference between high- and low-frequency limits of σ' , which is largest in the case of
 505 a pure Stern-layer polarization ($p = 1$). In contrast, in the case of a sole diffuse-layer
 506 polarization ($p = 0$), we hardly recognize any variation of σ' with the angular frequency.

507 The peak imaginary conductivity σ'' (Figure 6b) increases almost linearly with p ,
 508 i.e., the charge density in the Stern layer. For the same surface-charge densities, the Stern-

509 layer polarization ($p = 1$) results in a maximum of σ'' , which is approximately an or-
510 der of magnitude larger than the peak produced by the corresponding diffuse-layer po-
511 larization ($p = 0$). From Figure 7, which shows a close-up of the small imaginary con-
512 ductivities generated in the case of a depopulated Stern layer, it is evident that even a
513 small fraction of 20% of positive charge located in the Stern layer produces a stronger
514 response than the other 80% located in the diffuse layer. It is worth mentioning that the
515 polarization magnitude (here in terms of the maximum of σ'') largely varies with the mo-
516 bility of the counter-ions in the Stern layer. In a separate analysis, we observed a dif-
517 ference between the magnitudes of the two polarization processes of two orders of mag-
518 nitude when a larger mobility of $\mu_S = \mu/2$ was assumed (not shown). This observa-
519 tion is in agreement with the results obtained earlier by Lesmes and Morgan (2001) and
520 confirms their conclusion that the Stern-layer polarization produces a much stronger fre-
521 quency dispersion than the diffuse-layer polarization.

522 For sufficiently small values of p , Figure 7 also shows that the contribution of the
523 diffuse-layer polarization results in a slight increase of the polarization magnitude and
524 the characteristic angular frequency (curves 1 and 3) as compared to the pure Stern-layer
525 polarization (curve 4). The latter is related to the higher characteristic frequency of the
526 diffuse-layer relaxation as a consequence of the shorter relaxation time, here $\tau_\alpha \approx \tau_S/2$
527 because $S \approx 1$.

528 The comparison of the corresponding curves in Figures 6 and 7 also serves as a mu-
529 tual validation of our finite-difference implementation and the new analytical approx-
530 imation for the coupled polarization response. For angular frequencies between 0.1 and
531 10^4 mrad/s, the relative deviation between analytical and numerical results is $< 0.3\%$
532 in the real part and $< 20\%$ in the imaginary part of the effective conductivity. Here,
533 the analytical approximation clearly underestimates the polarization magnitude. A good
534 agreement, however, is observed between the characteristic frequency, i.e., the angular
535 frequency at which the σ'' peaks are observed. Apart from the underestimated polar-
536 ization magnitude, the good agreement between numerical and analytical curves confirms
537 the approach to model the coupled polarization process by a simple superposition of the
538 individual responses of Stern and diffuse layer.

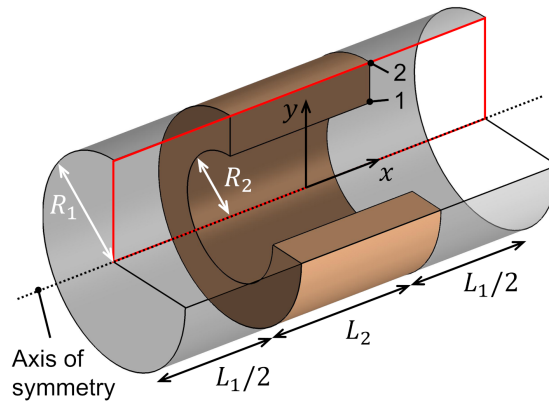


Figure 8. Three-dimensional sketch of the geometrical set-up used for the numerical simulation of membrane polarization in a pore constriction. The two wide cylinders of length $L_1/2$ and radius R_1 and the narrow cylinder of length L_2 and radius R_2 are saturated with electrolyte solution. The volume around the narrow cylinder belongs to the non-conducting matrix with dielectric constant ϵ_i . The red rectangle marks the actual two-dimensional model domain.

4 Membrane Polarization

Besides the polarization of Stern and diffuse layer around grains, the polarization of ion-selective pore constrictions can also cause a low-frequency dispersion of the complex conductivity. In the present section, we study this membrane-polarization mechanism based on an alternating series of wide and narrow cylinders. The cylinder walls are negatively charged and covered by an EDL consisting of a Stern and a diffuse layer, both contributing to the macroscopic polarization of the system. In order to assess their relative contributions, effective conductivity spectra are computed for varying charge densities in the two layers. Because no analytical model is available for the coupled response in this geometry, we resort to the numerical finite-element implementation validated in the previous section. We also show that after a slight modification presented here, the analytical membrane-polarization model proposed by Bückner and Hördt (2013a) reproduces the numerical results for the sole diffuse-layer polarization fairly well.

4.1 Analytical Model for Diffuse-Layer Polarization

Bückner and Hördt (2013a) considered the sequence of wide and narrow pores sketched in Figure 8. The pores are characterized by their radii R_i and lengths L_i ; the indices 1

and 2 denote properties of the wide and the narrow pore, respectively. A non-zero ζ -potential at the cylinder walls causes diffuse layers to build up. According to Bückner and Hördt (2013a), upon excitation by an external electrical field, the electrical current parallel to the symmetry axis will be controlled by the mean ion concentrations

$$b_{\pm,i} = \frac{2\pi}{C_{\pm}^{\infty} A_1} \int_0^{R_i} r C_{\pm,i}^{(0)}(r) dr. \quad (39)$$

These mean ion concentrations are averaged over the pore cross section and normalized with the bulk ion concentration C_{\pm}^{∞} . An additional normalization with the area of the wide pore $A_1 = \pi R_1^2$ accounts for the reduction of the total current through the narrow pore due to the reduced cross section (see Bückner & Hördt, 2013a).

For sufficiently small ζ -potentials, i.e., $\zeta \ll k_B T/e$, the radial variation of the electrical potential in the pore can be approximated by solving the linearized Poisson-Boltzmann equation in cylindrical coordinates, which gives (Hunter, 1981; Bückner & Hördt, 2013a)

$$U_a^{(0)}(r) = \zeta \frac{J_0(i\kappa r)}{J_0(i\kappa R)}, \quad (40)$$

where J_0 is the Bessel function of the first kind and order zero. The radial variation of the ion concentrations $C_{\pm,i}^{(0)}(r)$ are obtained by inserting $U_a^{(0)}(r)$ into equation 6.

For the typically much higher ζ -potential values of up to -100 mV on silica surfaces (here, $\Sigma = -0.01$ C/m²), the solution of the linearized Poisson-Boltzmann equation becomes imprecise. If we instead limit our treatment to sufficiently wide pore radii, i.e., $\kappa R_i \gg 1$, we can make use of Bikerman's equation 26, which is more adequate for highly charged surfaces. The dimensionless mean ion concentrations can then be approximated by

$$b_{\pm,i} \approx \frac{A_i}{A_1} \left(\frac{\pm 2\Sigma_{d\pm}^{(0)}}{e C_{\pm}^{\infty} R_i} + 1 \right). \quad (41)$$

Either of these definitions of $b_{\pm,i}$, i.e., equation 39 proposed by Bückner and Hördt (2013a) or equation 41 proposed here, can be used to express the effective transference numbers

$$t_{\pm,1} = \frac{b_{\pm,i}}{b_{+,i} + b_{-,i}}. \quad (42)$$

By means of this approximation, the three-dimensional cylindrical pore system is collapsed to a sequence of one-dimensional pores, the frequency-dependent impedance of which was derived by Marshall and Madden (1959). Following Bückner and Hördt (2013b)

and Bücker et al. (2017), the Marshall-Madden impedance can be written as

$$Z(\omega) = \frac{2}{\sigma_a} \left[\frac{L_1}{b_{+,1} + b_{-,1}} + \frac{L_2}{b_{+,2} + b_{-,2}} + \frac{8D(t_{+,1} - t_{+,2})^2}{\frac{L_1}{\tau_1} \sqrt{i\omega\tau_1} \coth \sqrt{i\omega\tau_1} + \frac{L_2}{\tau_2} \sqrt{i\omega\tau_2} \coth \sqrt{i\omega\tau_2}} \right], \quad (43)$$

where the frequency dependence is controlled by the two time constants

$$\tau_i = \frac{L_i^2}{2D} S_i \quad \text{with} \quad S_i = \frac{1}{4b_{+,i}t_{-,i}}. \quad (44)$$

In order to stress the structural similarities between these two relaxation times and the relaxation time of the diffuse layer around spherical grains, we can rewrite the dimensionless mean ion concentrations $b_{\pm,i}$ defined in equation 41 in terms of a Dukhin number for cylindrical geometries, which we define as

$$Du(\zeta, R_i) = \frac{\sigma_d(R_i)}{2\sigma_a} = \frac{|\sigma_{d+}(R_i) + \sigma_{d-}(R_i)|}{2\sigma_a}. \quad (45)$$

In analogy to equation 25, the surface conductivities write $\sigma_{d\pm}(R_i) = \pm 2\mu\Sigma_{d\pm}^{(0)}/R_i$. The coefficients S_i take the form

$$S_i = \frac{A_1}{2A_i} \frac{[2Du(\zeta, R_i) + 1]\sigma_a^2}{[2\sigma_{d+}(R_i) + 1][2\sigma_{d-}(R_i) + 1]}. \quad (46)$$

Besides the factor $A_1/(2A_i)$ and the factors 2, with which the Dukhin numbers and the individual conductivities $\sigma_{d\pm}$ are multiplied, this definition of S_i is equivalent to the definition of S in equation 34, which controls the relaxation time of the diffuse layer around spherical particles.

4.2 Numerical Model for the Coupled Polarization

The numerical modelling is carried out using COMSOL Multiphysics. Again, the cylindrical symmetry of the problem permits limiting the computation to a two-dimensional model domain (red rectangle in Figure 8). The systems of partial differential equations describing the static and the frequency-dependent parts of the polarization problem remain unchanged and only boundary conditions and finite-element mesh need to be adapted to the different geometry.

The boundary conditions for the static solution, i.e., equations 14 and 15, merge into $U^{(0)} = 0$ on the left and right boundary; $[\varepsilon_0\varepsilon_i\nabla U_i^{(0)} - \varepsilon_0\varepsilon_a\nabla U_a^{(0)}]\mathbf{n} = -\Sigma_d^{(0)}$ on the solid-liquid interface; and $\partial U(0)/\partial y = 0$ on the axis of symmetry and the entire top boundary. This set-up represents a discontinuous EDL, which only covers the surfaces

of the volume shown in brown in Figure 8. Additionally, we compute the response of a set-up, where the EDL is continuous in the wide pore and the boundary condition on the corresponding parts of the top boundary writes $[-\varepsilon_0\varepsilon_a\nabla U_a^{(0)}]\mathbf{n} = -\Sigma_d^{(0)}$.

For the frequency-dependent part of the problem, the boundary conditions described in equations 16 through 20 are adjusted as follows: $\delta n_{\pm} = 0$ and $\delta U_a = \pm E_0 L$ on the left and right boundary, respectively; $\mathbf{J}_{\pm} = 0$ and $\partial\delta U/\partial y = 0$ on the axis of symmetry and the top boundary; equations 18 through 20 remain unchanged on the solid-liquid interface. In the set-up with the continuous EDL, the boundary conditions on those parts of the top boundary, which delimit the wide pore, are given by the unchanged zero-flux condition 19 and the continuity of the displacement current, which here writes $-\varepsilon_0\varepsilon_a\nabla\delta U_a(\mathbf{r}_S)\cdot\mathbf{n} = \delta\Sigma_S(\mathbf{r}_S)$.

In order to avoid artifacts related to sharp corners covered by an EDL, the vertex 1 in Figure 8 is rounded off for the model with a discontinuous EDL, whereas the vertices 1 and 2 are rounded off for the model with a continuous EDL. In both cases, the radius of curvature is $(R_1 - R_2)/2$. For further technical details on the implementation, see the appendix.

The effective conductivity of the model can be obtained from numerically integrating the total ion flux densities through the left (or right) boundary. The resulting expression is equal to equation 37, if L substituted by R_1 . In the model with the continuous EDL, the surface current through the Stern layer has to be considered, too. The corresponding conductivity increment $-2/(E_0 R_1)[D_S\partial\delta\Sigma_S/\partial y + \mu_S\Sigma_S\partial\delta U_S/\partial y]$ has to be added to σ_{mod}^* . The analytical expression for the effective conductivity writes $\sigma_{\text{eff}}(\omega) = (L_1 + L_2)/Z(\omega)$, where $Z(\omega)$ is defined in equation 43.

4.3 Comparison of Analytical and Numerical Solution

The effective-conductivity spectra obtained from the model with the discontinuous EDL are shown in Figure 9. In the analytical models (for the case $p = 0$), the absence of the EDL in the wide pore has to be taken into account by setting $b_{\pm,1} = 1$ instead of using equation 39 or 41. The length of the narrow pore $L_2 = 10 \mu\text{m}$ was selected to match the diameter of the spherical particle treated above; the length of the wide pore $L_1 = 90 \mu\text{m}$ as well as the two pore radii $R_1 = 2 \mu\text{m}$ and $R_2 = 0.2 \mu\text{m}$ were adjusted to achieve a significant polarization response. As discussed in more de-

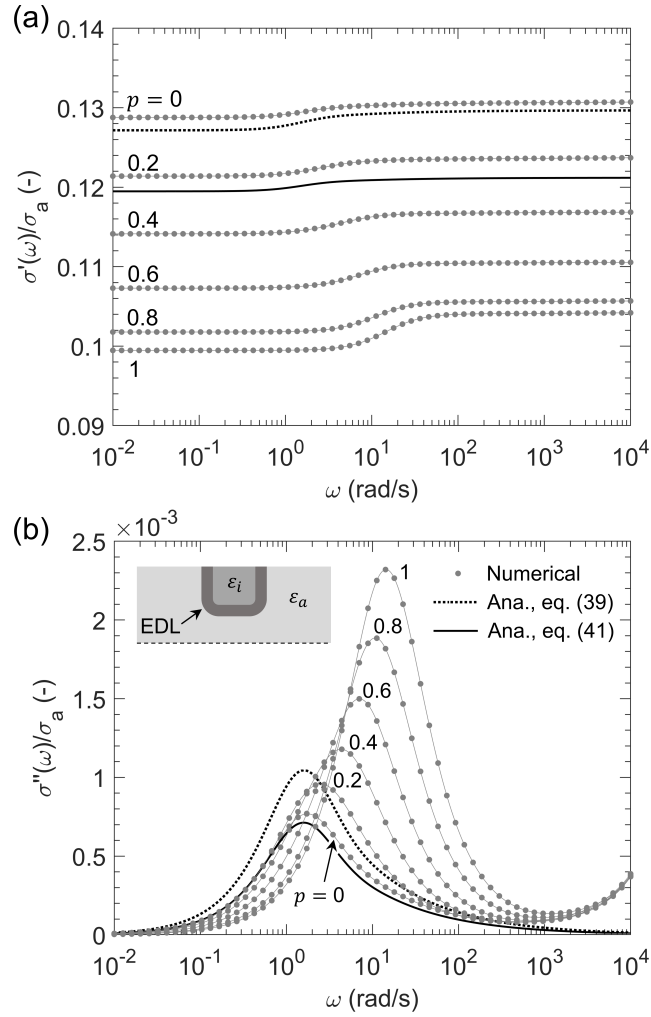


Figure 9. Complex-conductivity spectra of the membrane-polarization model for different ratios $p = -\Sigma_S^{(0)}/\Sigma$. Complex-valued conductivity in terms of real (a) and imaginary parts (b) normalized to the bulk conductivity σ_a . Numerical results (grey circles, lines are to guide the eye only) for all values of p are displayed along with the analytical models for $p = 0$ after Bückner and Hördt (2013a) using the average ion concentrations from equation 39 (dotted line) and from equation 41 (solid line). The sketch in (b) shows that the EDL is discontinuous in the wide pore. Pore lengths and radii are $L_1 = 90 \mu\text{m}$, $L_2 = 10 \mu\text{m}$, $R_1 = 2 \mu\text{m}$, and $R_2 = 0.2 \mu\text{m}$; all other parameter values are the same as in Figure 6.

643 tail in Hördt et al. (2017), the polarization magnitude of the model by Bückner and Hördt
 644 (2013a) largely depends on the relation between the two ratios R_1/R_2 and L_1/L_2 .

645 In Figure 9a, we observe a similar variation of the magnitude of σ' with the ratio
 646 p as for the polarization around a spherical particle. In both cases, the surface conduc-
 647 tivity increases σ' if the counter-charges are mainly located in the diffuse layer. At low
 648 frequencies, the Stern layer polarizes and does not contribute to σ' ; at high frequencies,
 649 its contribution is limited by the low ion mobility in the Stern layer (remember that $\mu_S =$
 650 $\mu/10$). Moreover, the variation of the imaginary part σ'' with p (Figure 9b) is similar
 651 to the one observed for the spherical particle. Again, the σ'' peak increases with the amount
 652 of counter-charges located in the Stern layer, i.e., with increasing p , and shifts towards
 653 higher angular frequencies.

654 Figure 9 also shows that computing the mean ion concentrations from equation 41
 655 instead of equation 39 improves the agreement with the numerical solution: for $p = 0$,
 656 the relative deviations between the analytical and the numerical σ'' curves are $< 20\%$
 657 for the modified and $< 50\%$ for the original model at angular frequencies < 100 rad/s.
 658 Because the analytical model does not consider Maxwell-Wagner polarization, which be-
 659 comes dominant at high frequencies, the misfit increases at angular frequencies > 100
 660 rad/s. The original membrane polarization model, however, matches the real part (σ')
 661 better. Here, the relative deviation between the analytical models and the numerical so-
 662 lution are $\approx 7\%$ for the modified and $< 1\%$ for the original model.

663 The fair overall agreement of analytical and numerical curves for $p = 0$ confirms
 664 the validity of the model developed by Bückner and Hördt (2013a) for a sole diffuse-layer
 665 polarization. The same authors also proposed a simple modification of the mean counter-
 666 ion concentration to take into account the contribution of the Stern layer. However, their
 667 model rather predicts a continuous decrease of the polarization magnitude with increas-
 668 ing p and practically a constant characteristic frequency (not shown here for brevity),
 669 indicating that the Stern-layer polarization is more complex than assumed by Bückner
 670 and Hördt (2013a).

671 The polarization response changes significantly if the EDL is assumed to be con-
 672 tinuous in the wide pore (Figure 10). Here, magnitude and characteristic frequency of
 673 the main σ'' peak located around 2 rad/s decrease only slightly from $p = 0$ through $p =$
 674 0.4 and increase not much steeper for larger values of p . In comparison to the significant

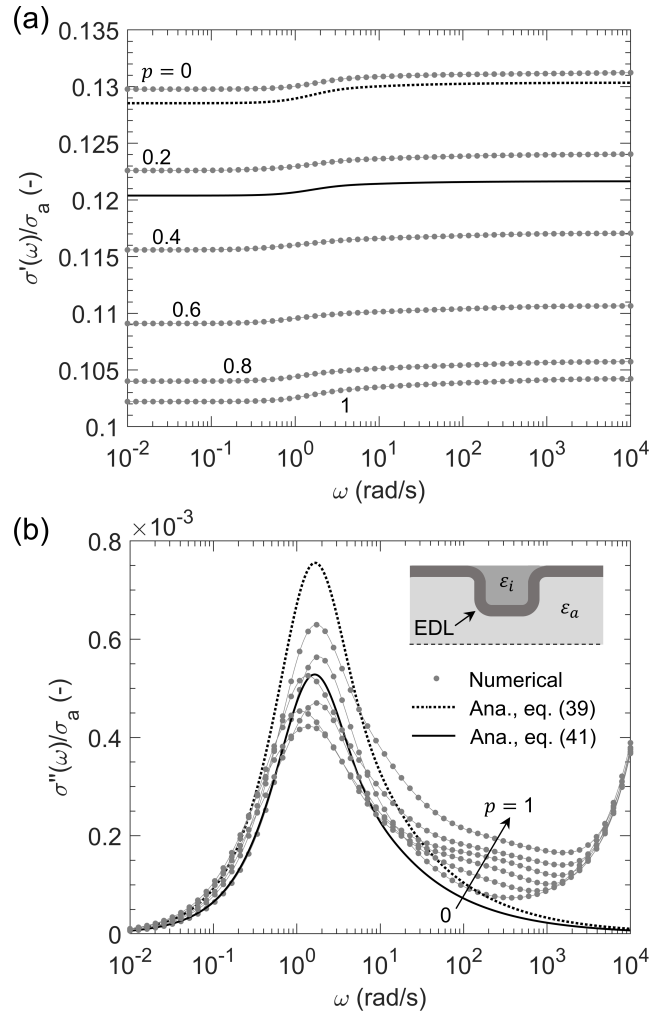


Figure 10. Complex-conductivity spectra of the membrane-polarization model with a continuous EDL in terms of the normalized real (a) and imaginary conductivity (b). Numerical results (grey circles, lines are to guide the eye only) for different values of p are displayed along with the analytical models for $p = 0$ after Bückner and Hördt (2013a) using the average ion concentrations from equation 39 (dotted line) and from equation 41 (solid line). The sketch in (b) shows the continuous EDL in the wide pore; all other parameter values are the same as in Figure 9.

675 variation of the main peak observed in Figure 9 for the discontinuous EDL, here, the σ''
676 peak remains almost unchanged. Furthermore, at frequencies between 100 and 1000 rad/s,
677 a smaller secondary polarization peak appears for $p > 0$ and increases monotonically
678 with p . The real part σ' shows the usual decrease of surface conductivity with increas-
679 ing p . The relative deviations between the numerical results for $p = 0$ and the two an-
680 analytical models are similar to those reported above for a discontinuous EDL.

681 5 Discussion

682 The new analytical model presented here describes Maxwell-Wagner, Stern-layer,
683 and diffuse-layer polarization around spherical grains and permits analyzing the frequency
684 response due to a superposition of all three mechanisms. Numerical and analytical re-
685 sults for typical model parameters consistently confirm the results of earlier studies: the
686 contribution of the diffuse-layer polarization to the macroscopic response is significantly
687 smaller than the one of the Stern-layer polarization (e.g., de Lima & Sharma, 1992; Lesmes
688 & Morgan, 2001). In most practical cases, the polarization of the diffuse layer can there-
689 fore safely be neglected.

690 The comparison of numerical and analytical results also confirmed the strong cou-
691 pling of the surface charge in the Stern layer with charges in the electrolyte as predicted
692 by Lyklema et al. (1983). The model proposed by Lyklema and co-workers can easily
693 be obtained from the model by Schwarz (1962) by adjusting the relaxation time of the
694 Stern layer: for a charge density in the Stern layer of $\Sigma_S^{(0)} \approx 0.01$ C/m² and a bulk ion
695 concentration of 1 mol/m³, equation 32 predicts a reduction of the relaxation time by
696 a factor $1/\approx 6.4$. This effect can also be interpreted in terms of an effective diffusion
697 coefficient $D_S^{\text{eff}} = D_S M$, which in our case (i.e., $D_S = D/10$) is only a factor ≈ 2 smaller
698 than the diffusion coefficient of the ions in the bulk electrolyte.

699 This observation is of particular interest as it offers an explanation for the large
700 diffusion coefficients D_S needed to adjust the model by Leroy et al. (2008) to measured
701 complex-conductivity spectra. The model by Leroy and co-workers does not include the
702 correction of the relaxation time proposed by Lyklema et al. (1983). Thus, it often re-
703 quires the assumption of similar diffusion coefficients in Stern layer and bulk electrolyte
704 (e.g., Leroy et al., 2008; Leroy & Revil, 2009; Revil & Florsch, 2010; Schmutz et al., 2010).
705 Independent determinations of the diffusion coefficient in the Stern layer from experi-

706 mental surface-conductivity and particle-mobility data, however, normally result in a re-
707 duction of the counter-ion mobility by a factor 10 or larger (e.g., Zukoski & Saville, 1986;
708 Revil & Glover, 1998). A recent extension of the model by Leroy et al. (2008) already
709 considers the corrected relaxation time and successfully adjusts the polarization response
710 of calcite precipitations on glass beads (Leroy et al., 2017). Together with our findings
711 that support the theory by Lyklema et al. (1983), this indicates that the difference be-
712 tween the predictions of the two experiments could be reduced significantly, if the Stern-
713 layer relaxation time used in the model by Leroy et al. (2008) (and subsequent studies)
714 was replaced by the one defined in equations 31 and 32.

715 Although the correction of the relaxation time might be able to justify the (to date)
716 unexplained assumption inherent to the model by Leroy et al. (2008), it also questions
717 the often-used simple relation between relaxation time and grain size by introducing an
718 additional dependence on chemical properties of pore fluid and solid surface: the coef-
719 ficient M strongly depends on the electrolyte concentration and the surface-charge den-
720 sity in the Stern layer. Consequently, besides the grain diameter and the diffusion co-
721 efficient in the Stern layer, variations of experimentally determined relaxation times might
722 partly be due to variations of these chemical parameters.

723 We have also applied our finite-element model to study membrane polarization, which
724 had not been investigated in the same detail as the polarization around spherical grains
725 before. In the limiting case of a sole diffuse-layer polarization, we found that an improved
726 analytical formulation based on the work by Marshall and Madden (1959) and Bückner
727 and Hördt (2013a) yields a good agreement with the numerical results. However, the an-
728 analytical model does not reproduce the numerical results for the coupled polarization of
729 diffuse and Stern layer. Consequently, the incorporation of the Stern-layer polarization
730 in the model by Bückner and Hördt (2013a) is insufficient in its current form and our nu-
731 merical results can contribute substantially to our understanding of the role of the Stern
732 layer in the context of membrane polarization.

733 Even in the pore-constriction geometry, the polarization of the Stern layer can con-
734 trol the frequency response, especially if the EDL is discontinuous. Certain similarities
735 of the coupled responses of both geometries stand out – namely the generally larger re-
736 sponse of the Stern-layer polarization and the simultaneous increase of characteristic fre-
737 quency and polarization magnitude with the surface charge in the Stern layer. However,

738 we also observed that the particular geometrical configuration of the EDL in the pore-
739 constriction model can largely reduce the difference between the respective magnitudes
740 of diffuse-layer and Stern-layer polarization: if the EDL becomes continuous, the con-
741 tributions of both mechanisms can become practically the same.

742 Although we have taken an important step towards this long-term goal, it is be-
743 yond the scope of the present study to provide an analytical model that integrates mem-
744 brane polarization and the polarization around spherical grains. Nevertheless, we can
745 put our results into a broader context and draw some preliminary conclusions regard-
746 ing the relative contributions of the various polarization mechanisms.

747 Grain-based polarization models are best suited for the modelling of dilute suspen-
748 sions of dielectric particles because they only account for grain-electrolyte interactions
749 and largely ignore grain-grain interactions. For practical purposes, these models can even
750 be applied to high particle concentrations and the responses of unconsolidated granu-
751 lar media (e.g., Leroy et al., 2008) have been matched successfully with this type of mod-
752 els. For typical parameter combinations, the polarization of isolated grains is only con-
753 trolled by the Stern layer and contributions of a simultaneously occurring diffuse-layer
754 polarization can be neglected.

755 With increasing degree of compaction and cementation, grain-grain interactions are
756 expected to become more important (e.g., Lesmes & Morgan, 2001). These interactions
757 include (i) the interaction of polarization dipoles of adjacent grains as well as (ii) per-
758 colating diffuse and Stern layers. Based on the good agreement between experimental
759 data and the responses of grain-based polarization models, the interaction of polariza-
760 tion dipoles can safely be neglected. To date, the effect of percolating diffuse and Stern
761 layers on the polarization response has only been touched in passing: for instance, Leroy
762 et al. (2008) argue that a diffuse layer above the percolation threshold cannot polarize
763 and only consider an increase of the low-frequency conductivity. In the same sense, they
764 postulate that the Stern layers of adjacent particles are discontinuous because the model
765 based on the Stern-layer polarization accurately describes experimental observations. While
766 the result of this argumentation – the small contribution of the diffuse-layer polariza-
767 tion and the dominating role of the Stern layer – agree with our findings, the physical
768 picture should be reconsidered: around isolated particles, the polarization of the diffuse
769 layer is negligible, too, such that it is not necessary to assume that the diffuse layers are

770 percolating. In addition, we have shown that even in the case of continuous (or perco-
771 lating) diffuse and Stern layers in the pore-constriction model, both layers can polarize.
772 Consequently, the discontinuity of neither of the two layers is needed to generate a po-
773 larization response.

774 The similarity of the polarization response of grain-based and pore-constriction ge-
775 ometry indicates a gradual transition between the two models with increasing degree of
776 compaction and cementation. As long as the EDLs are assumed to be discontinuous, the
777 Stern layer dominates the polarization response of both models, which makes the dis-
778 tinction between effects related to individual grains and effects related to pore constrict-
779 tions a mere question of the point of view. Our results suggest that responses caused by
780 pore constrictions, i.e., typical membrane-polarization responses, can – at least to a cer-
781 tain degree – be adjusted using grain-based models and vice versa. This is particularly
782 plausible, if we consider that in granular media made of near-spherical particles, pore
783 diameters and pore lengths are of the same order of magnitude as the typical grain sizes
784 and thus all relaxation times are controlled by similar characteristic lengths.

35 **6 Conclusions**

786 We have investigated the low-frequency electrical conductivity of porous media by
787 means of analytical and numerical models for single-grain and pore-constriction geome-
788 tries. Our results allowed us to assess the relative contributions of polarization mech-
789 anisms originating from the diffuse part and the Stern layer of the EDL covering charged
790 mineral surfaces. Because our models also include Maxwell-Wagner polarization, they
are useful for a broad frequency range.

792 To match our numerical results, we assembled a new analytical model for the grain-
793 based geometry by combining the Dukhin-Shilov model (Dukhin & Shilov, 1974), which
794 accounts for the diffuse-layer polarization, with Schurr’s Stern-layer polarization model
795 (Schurr, 1964) including a correction of the Stern-layer relaxation time proposed by Lyklema
796 et al. (1983). The corrected relaxation time, which accounts for the interaction of the
797 charges in the Stern layer with the electrolyte solution, significantly improves the agree-
798 ment of analytical and numerical results. Without the correction, untypically high dif-
799 fusion coefficients of the counter-ions in the Stern layer have to be assumed to fit the spec-
800 tral response. For typical model parameters, the relative contribution of the diffuse-layer

polarization was seen to be insignificant in comparison to the large response of the Stern layer.

Our numerical results for the pore-constriction geometry agree with the analytical membrane-polarization model by Bückner and Hördt (2013a) if we relate the mean ion concentrations of the cylindrical pores to Bikerman's expression for the surface conductivity of highly charged surfaces (Bikerman, 1933) and as long as no Stern layer is considered. We also propose detailed model to describe Stern-layer polarization in a typical membrane-polarization geometry. As in the grain-based model, the diffuse layer makes a much smaller contribution to the total response than the Stern layer – at least as long as the charged surfaces are below the percolation threshold, i.e., the individual EDLs are not interconnected at the system scale.

In conclusion, the responses of grain-based and pore-constriction geometries are more similar than usually assumed, particularly if the polarization of both parts of the EDL are taken into account. Below the percolation threshold, the Stern-layer dominates the macroscopic response, but as soon as the EDL becomes percolating, this dominance breaks down and both mechanisms contribute to a similar extend. More detailed studies on specific pore geometries are required to conclusively assess the relative importance of the different polarization mechanisms, but our study is a significant step towards this long-term goal and sets the basis for extensive numerical studies.

Appendix A Numerical Implementation

The COMSOL partial differential equation (PDE) interface in coefficient form allows the definition of PDEs and systems of PDEs of the general type

$$e_a \frac{\partial^2 u}{\partial t^2} + d_a \frac{\partial u}{\partial t} + \nabla \cdot (-c \nabla u - \alpha u + \gamma) + \beta \cdot \nabla u + a u = f \quad (\text{A1})$$

with the general boundary conditions

$$-\mathbf{n} \cdot (-c \nabla u - \alpha u + \gamma) = g - q u \quad \text{and} \quad (\text{A2})$$

$$u = s, \quad (\text{A3})$$

where u denotes the dependent variable and \mathbf{n} the inward-pointing unit normal vector.

Due to their cylindrical symmetry, the problems can be solved on two-dimensional domains (see Figures 5 and 8) with coordinates $\mathbf{r} = (x, y)^T$ and gradient operator $\nabla =$

($\partial/\partial x, \partial/\partial y$)^T. As explained in more detail in Bücke et al. (2018), multiplying all coefficients in equations A1 and A2 by y yields a transformation to cylindrical coordinates.

A1 Static Solution

The static problem set up by equations 6 and 7 is implemented by setting $u_1 = U^{(0)}(\mathbf{r})$, $c_1 = y\varepsilon_0\varepsilon_a$, $f_1 = -y2C_{\pm}^{\infty}e\sinh(u_1e/(kT))$ in the electrolyte as well as $c_1 = y\varepsilon_0\varepsilon_a$ and $f_1 = 0$ in the solid phase. Note that in this appendix, coefficients are assumed to be zero if not specified differently.

The fixed surface-charge boundary condition 15 is realized by setting $g = -y\Sigma_d^{(0)}$ on all charged boundaries. The definition of the zero reference potential, equation 14, depends on the specific model: In the grain geometry, we set $s = 0$ on the left, right, and top boundary; in the membrane geometry, we define the point-wise constraint $u_1 = 0$ at two positions ($x = \pm(L_1 + L_2)/2, y = 0$) located on the left and right boundary, respectively. In this case, standard no-flow boundary conditions are set on the remaining parts of left and right boundary, as well as on the uncharged parts of the top boundary. Because $y = 0$ is the symmetry axis (selecting rotational symmetry in the model set-up), no specific boundary conditions are defined on this boundary.

A2 Frequency-Dependent Solution

For the frequency-dependent problem set up by the coupled PDEs 8 and 9, which describe the physics in the electrolyte, the Laplace equation 13, which controls the electrical field in the solid phase, and equation 11, which controls the surface charge in the Stern layer, need to be solved simultaneously. We use the same dependent variable u_2 in the electrolyte and in the solid phase and define suitable PDE coefficients on each of the two subdomains. The variable u_2 writes

$$\mathbf{u}_2 = \begin{bmatrix} u_{21} \\ u_{22} \\ u_{23} \end{bmatrix} = \begin{bmatrix} \delta C_{-}(\mathbf{r}, \omega) \\ \delta C_{+}(\mathbf{r}, \omega) \\ \delta U(\mathbf{r}, \omega) \end{bmatrix}. \quad (\text{A4})$$

Assuming isotropic properties, the coefficient c_2 is a 3-by-3 coefficient matrix. In the electrolyte it writes

$$c_2 = \begin{bmatrix} yD & 0 & -y\mu C_-^\infty \exp(\frac{e}{kT}u_1) \\ 0 & yD & y\mu C_+^\infty \exp(-\frac{e}{kT}u_1) \\ 0 & 0 & y\varepsilon_0\varepsilon_a \end{bmatrix} \quad (\text{A5})$$

and in the solid phase

$$c_2 = \begin{bmatrix} 0 & 0 & 0 \\ 0 & 0 & 0 \\ 0 & 0 & y\varepsilon_0\varepsilon_i \end{bmatrix}. \quad (\text{A6})$$

The variable u_1 is the static part of the electrical potential. The coefficient matrix $\underline{\alpha}$ writes

$$\underline{\alpha}_2 = \begin{bmatrix} -y\mu\nabla u_1 & 0 & 0 \\ 0 & y\mu\nabla u_1 & 0 \\ 0 & 0 & 0 \end{bmatrix}, \quad (\text{A7})$$

in the electrolyte and is equal to the null matrix in the solid phase. Note that on our two-dimensional modelling domain, each element of the matrix $\underline{\alpha}_2$ is a two-element vector.

The matrix \underline{a}_2 is

$$\underline{a}_2 = \begin{bmatrix} yi\omega & 0 & 0 \\ 0 & yi\omega & 0 \\ yF & -yF & 0 \end{bmatrix} \quad (\text{A8})$$

in the electrolyte. In the solid phase, \underline{a}_2 is the same except for the last line, which has to be filled with zeros instead.

Equation 11 describing the perturbation surface-charge density $\delta\Sigma_S$ is solved on the solid-liquid interface only. By means of a so-called lower-dimensional physics interface, the curvature of this interface is taken into account. Because the electrical potential in the Stern layer has to be equal to the potentials δU_i and δU_a on the corresponding boundaries, the only dependent variable on the interface is $u_3 = \delta\Sigma_S(\mathbf{r}_S, \omega)$. The coefficients are $c_3 = yD_S$, $a_3 = yi\omega$, and $\gamma_3 = -y\mu_S\Sigma_S^{(0)}\nabla u_{23}$, where u_{23} denotes the perturbation potentials on the adjacent two-dimensional subdomains.

The boundary condition 16 describing the external excitation and the condition on the perturbation concentrations 17 are realized by setting $\mathbf{s}_2 = (0, 0, \pm E_0 L)^T$. In the membrane-polarization model with the continuous EDL, this boundary is not located at a far distance from the charged surface. However, because of the symmetry of the problem with respect to $x = 0$, we expect the perturbation ion concentrations to vanish in

879 this geometry, too (see e.g., concentration profiles in Blaschek & Hördt, 2009). For the
 880 same reason, the perturbation surface-charge density $\delta\Sigma_S$ is also expected to vanish on
 881 the left and right boundary and we set $s_3 = 0$ (only for a continuous EDL).

882 On the solid-liquid interface, we implement the zero-flux boundary conditions 19
 883 and the condition on the displacement current 20 by defining $\mathbf{g} = (0, 0, yu_3)^T$.

884 On the top boundary, we implement zero-flux boundary condition on all three com-
 885 ponents of u_2 resulting in vanishing normal ion fluxes and a vanishing normal electri-
 886 cal field. In the membrane-polarization model with the continuous EDL, parts of the top
 887 boundary represent charged surfaces and are furnished with the corresponding bound-
 888 ary conditions described above. In the membrane-polarization model with the discon-
 889 tinuous EDL, the one-dimensional domain representing the Stern layer ends at the top
 890 boundary. In this case, we also define no-flux boundary conditions for u_3 .

891 A3 Model Discretization

892 Special care has to be taken with the model discretization: while particle and sizes
 893 are in the micro- to millimeter range, the thickness of the diffuse layer is orders of mag-
 894 nitude smaller. We use a special quadrangle boundary-layer mesh at the solid-liquid in-
 895 terface, which in radial direction consists of 8 elements with sizes increasing from $\lambda_D/2$
 896 at the surface to $\approx 1.8\lambda_D$ at the outer edge. In tangential direction (i.e., along the bound-
 897 aries), the elements have a size of $\pi a/400$ in the grain-based model and $R_2/5$ in the pore-
 898 constriction geometry. The remaining volume is filled with triangular elements, the max-
 899 imum size of which increases from $\pi a/400$ (or $R_2/5$) at the edge of the boundary-layer
 900 meshes to $L/20$ (or $R_1/5$) at the remote boundaries. For a spherical particle of radius
 901 $a = 5 \mu\text{m}$, this results in a total of ≈ 20900 elements, of which 6400 elements corre-
 902 spond to the boundary-layer mesh. For pore lengths $L_1 = 90 \mu\text{m}$ and $L_2 = 10 \mu\text{m}$ and
 903 pore radii $R_1 = 2 \mu\text{m}$ and $R_2 = 0.2 \mu\text{m}$, the meshes consist of ≈ 14700 elements (\approx
 904 11000 for the continuous EDL), of which ≈ 5200 (≈ 7600) elements make the boundary-
 905 layer mesh.

906 Acknowledgments

907 M. Bückler acknowledges the Austrian Federal Ministry of Science, Research and Econ-
 908 omy (project: Development of geophysical exploration methods for the characterization

of mine-tailings towards exploitation) and the German Academic Exchange Service (DAAD) for scholarships received for his work on this study. All authors gratefully acknowledge P. Leroy and one anonymous reviewer for their insightful comments that helped to improve the manuscript. Scripts, numerical models, and data used for this manuscript are available at Zenodo (DOI:10.5281/zenodo.3067277).

References

- Atekwana, E. A., & Slater, L. D. (2009). Biogeophysics: A new frontier in earth science research. *Reviews of Geophysics*, *47*(4).
- Atkins, P., & De Paula, J. (2013). *Elements of physical chemistry*. Oxford University Press, USA.
- Bairlein, K., Bückner, M., Hördt, A., & Hinze, B. (2016). Temperature dependence of spectral induced polarization data: experimental results and membrane polarization theory. *Geophysical Journal International*, *205*(1), 440–453.
- Bikerman, J. (1933). Iontheorie der Elektromose, der Strömungsströme und der Oberflächenleitfähigkeit. *Z. Physikalische Chemie A*, *163*, 378–394.
- Blaschek, R., & Hördt, A. (2009). Numerical modelling of the ip effect at the pore scale. *Near Surface Geophysics*, *7*(5-6), 579-588.
- Börner, F., Schopper, J., & Weller, A. (1996). Evaluation of transport and storage properties in the soil and groundwater zone from induced polarization measurements. *Geophysical Prospecting*, *44*(4), 583–601.
- Bruggeman, D. A. G. (1935). Berechnung verschiedener physikalischer Konstanten von heterogenen Substanzen. I. Dielektrizitätskonstanten und Leitfähigkeiten der Mischkörper aus isotropen Substanzen. *Annalen der Physik*, *416*(7), 636–664.
- Buchheim, W., & Irmer, G. (1979). Zur Theorie der induzierten galvanischen Polarisation in Festkörpern mit elektrolytischer Porenfüllung. *Gerlands Beitr. Geophysik*, *88*, 53-72.
- Bückner, M., & Hördt, A. (2013a). Analytical modelling of membrane polarization with explicit parametrization of pore radii and the electrical double layer. *Geophysical Journal International*, ggt136.
- Bückner, M., & Hördt, A. (2013b). Long and short narrow pore models for membrane polarization. *Geophysics*, *78*(6), E299–E314.

- 941 Bückner, M., Orozco, A. F., Hördt, A., & Kemna, A. (2017). An analytical
942 membrane-polarization model to predict the complex conductivity signature of
943 immiscible liquid hydrocarbon contaminants. *Near Surface Geophysics*, *15*(6),
944 547–562.
- 945 Bückner, M., Undorf, S., Flores Orozco, A., & Kemna, A. (2018). Electro-chemical
946 polarization around metallic particles-part 2: The role of diffuse surface charge.
947 *Geophysics*, *84*(2), 1–64.
- 948 Chew, W., & Sen, P. (1982a). Dielectric enhancement due to electrochemical dou-
949 ble layer: thin double layer approximation. *The Journal of Chemical Physics*,
950 *77*(9), 4683–4693.
- 951 Chew, W., & Sen, P. (1982b). Potential of a sphere in an ionic solution in thin dou-
952 ble layer approximations. *The Journal of Chemical Physics*, *77*(4), 2042–2044.
- 953 DeLacey, E. H., & White, L. R. (1981). Dielectric response and conductivity of di-
954 lute suspensions of colloidal particles. *Journal of the Chemical Society, Fara-
955 day Transactions 2: Molecular and Chemical Physics*, *77*(11), 2007–2039.
- 956 de Lima, O. A., & Sharma, M. M. (1992). A generalized Maxwell-Wagner theory for
957 membrane polarization in shaly sands. *Geophysics*, *57*(3), 431–440.
- 958 Dukhin, S., & Shilov, V. (1974). *Dielectric phenomena and the double layer in dis-
959 perse systems and polyelectrolytes*. Wiley, New York.
- 960 Fixman, M. (1980). Charged macromolecules in external fields. I. The sphere. *The
961 Journal of Chemical Physics*, *72*(9), 5177–5186.
- 962 Flores Orozco, A., Williams, K. H., Long, P. E., Hubbard, S. S., & Kemna, A.
963 (2011). Using complex resistivity imaging to infer biogeochemical processes
964 associated with bioremediation of an uranium-contaminated aquifer. *Journal
965 of Geophysical Research: Biogeosciences*, *116*(G3).
- 966 Fridrikhsberg, D., & Sidorova, M. (1961). A study of relationship between the in-
967 duced polarization phenomenon and the electro-kinetic properties of capillary
968 systems (in Russian). *Vestnik Leningradskogo Universiteta, Seria Chimia*, *4*,
969 222–226.
- 970 Garcia, A., Grosse, C., & Brito, P. (1985). On the effect of volume charge dis-
971 tribution on the Maxwell-Wagner relaxation. *Journal of Physics D: Applied
972 Physics*, *18*(4), 739.
- 973 Grahame, D. C. (1947). The electrical double layer and the theory of electrocapillar-

- 974 ity. *Chemical reviews*, *41*(3), 441–501.
- 975 Grosse, C., & Shilov, V. N. (1996). Theory of the low-frequency electrorotation
976 of polystyrene particles in electrolyte solution. *The Journal of Physical Chem-*
977 *istry*, *100*(5), 1771–1778.
- 978 Hanai, T. (1960). Theory of the dielectric dispersion due to the interfacial polariza-
979 tion and its application to emulsions. *Kolloid-Zeitschrift*, *171*(1), 23–31.
- 980 Hinch, E. J., Sherwood, J. D., Chew, W. C., & Sen, P. N. (1984). Dielectric re-
981 sponse of a dilute suspension of spheres with thin double layers in an asym-
982 metric electrolyte. *Journal of the Chemical Society, Faraday Transactions 2:*
983 *Molecular and Chemical Physics*, *80*(5), 535–551.
- 984 Hördt, A., Bairlein, K., Bielefeld, A., Bücken, M., Kuhn, E., Nordsiek, S., & Stebner,
985 H. (2016). The dependence of induced polarization on fluid salinity and pH,
986 studied with an extended model of membrane polarization. *Journal of Applied*
987 *Geophysics*.
- 988 Hördt, A., Bairlein, K., Bücken, M., & Stebner, H. (2017). Geometrical constraints
989 for membrane polarization. *submitted to Near Surface Geophysics*.
- 990 Hördt, A., Druiventak, A., Blaschek, R., Binot, F., Kemna, A., Kreye, P., & Zisser,
991 N. (2009). Case histories of hydraulic conductivity estimation with induced
992 polarization at the field scale. *Near Surface Geophysics*, *7*(5-6), 529–545.
- 993 Hunter, R. (1981). *Zeta potential in colloid science: Principles and applications*.
994 Academic Press, London.
- 995 Kemna, A., Binley, A., Cassiani, G., Niederleithinger, E., Revil, A., Slater, L., . . .
996 others (2012). An overview of the spectral induced polarization method for
997 near-surface applications. *Near Surface Geophysics*, *10*(6), 453–468.
- 998 Kijlstra, J., van Leeuwen, H. P., & Lyklema, J. (1992). Effects of surface conduc-
999 tion on the electrokinetic properties of colloids. *Journal of the Chemical Soci-*
1000 *ety, Faraday Transactions*, *88*(23), 3441–3449.
- 1001 Kosmulski, M. (2006). Electric charge density of silica, alumina, and related sur-
1002 faces. In P. Somasundaran (Ed.), *Encyclopedia of surface and colloid science*
1003 (Vol. 3, p. 1857-1867). New York, London: CRC press.
- 1004 Leroy, P., Li, S., Jougnot, D., Revil, A., & Wu, Y. (2017). Modelling the evolution
1005 of complex conductivity during calcite precipitation on glass beads. *Geophysi-*
1006 *cal Journal International*, *209*(1), 123–140.

- 1007 Leroy, P., & Revil, A. (2004). A triple-layer model of the surface electrochemical
1008 properties of clay minerals. *Journal of Colloid and Interface Science*, *270*(2),
1009 371–380.
- 1010 Leroy, P., & Revil, A. (2009). A mechanistic model for the spectral induced po-
1011 larization of clay materials. *Journal of Geophysical Research: Solid Earth*,
1012 *114*(B10).
- 1013 Leroy, P., Revil, A., Kemna, A., Cosenza, P., & Ghorbani, A. (2008). Complex con-
1014 ductivity of water-saturated packs of glass beads. *Journal of Colloid and Inter-
1015 face Science*, *321*(1), 103–117.
- 1016 Lesmes, D. P., & Morgan, F. D. (2001). Dielectric spectroscopy of sedimentary
1017 rocks. *Journal of Geophysical Research: Solid Earth*, *106*(B7), 13329–13346.
- 1018 Lyklema, J., Dukhin, S., & Shilov, V. (1983). The relaxation of the double layer
1019 around colloidal particles and the low-frequency dielectric dispersion: Part I.
1020 Theoretical considerations. *Journal of Electroanalytical Chemistry and Interfa-
1021 cial Electrochemistry*, *143*(1-2), 1–21.
- 1022 Marshall, D. J., & Madden, T. R. (1959). Induced polarization, a study of its
1023 causes. *Geophysics*, *24*(4), 790–816.
- 1024 Maxwell, J. C. (1892). *A treatise on electricity and magnetism* (3rd ed.). Clarendon,
1025 Oxford, England.
- 1026 O’Konski, C. T. (1960). Electric properties of macromolecules. V. Theory of ionic
1027 polarization in polyelectrolytes. *The Journal of Physical Chemistry*, *64*(5),
1028 605–619.
- 1029 Revil, A., Cathles, L., Losh, S., & Nunn, J. (1998). Electrical conductivity in shaly
1030 sands with geophysical applications. *Journal of Geophysical Research: Solid
1031 Earth*, *103*(B10), 23925–23936.
- 1032 Revil, A., & Florsch, N. (2010). Determination of permeability from spectral in-
1033 duced polarization in granular media. *Geophysical Journal International*,
1034 *181*(3), 1480–1498.
- 1035 Revil, A., & Glover, P. (1997). Theory of ionic-surface electrical conduction in
1036 porous media. *Physical Review B*, *55*(3), 1757.
- 1037 Revil, A., & Glover, P. (1998). Nature of surface electrical conductivity in natural
1038 sands, sandstones, and clays. *Geophysical Research Letters*, *25*(5), 691–694.
- 1039 Robinson, D., & Friedman, S. (2003). A method for measuring the solid particle per-

- 1040 mittivity or electrical conductivity of rocks, sediments, and granular materials.
1041 *Journal of Geophysical Research: Solid Earth*, 108(B2).
- 1042 Schmutz, M., Revil, A., Vaudelet, P., Batzle, M., Viñao, P. F., & Werkema, D.
1043 (2010). Influence of oil saturation upon spectral induced polarization of oil-
1044 bearing sands. *Geophysical Journal International*, 183(1), 211–224.
- 1045 Schurr, J. (1964). On the theory of the dielectric dispersion of spherical colloidal
1046 particles in electrolyte solution. *The Journal of Physical Chemistry*, 68(9),
1047 2407–2413.
- 1048 Schwarz, G. (1962). A theory of the low-frequency dielectric dispersion of colloidal
1049 particles in electrolyte solution. *The Journal of Physical Chemistry*, 66(12),
1050 2636–2642.
- 1051 Shilov, V., Delgado, A., Gonzalez-Caballero, F., & Grosse, C. (2001). Thin double
1052 layer theory of the wide-frequency range dielectric dispersion of suspensions of
1053 non-conducting spherical particles including surface conductivity of the stag-
1054 nant layer. *Colloids and Surfaces A: Physicochemical and Engineering Aspects*,
1055 192(1), 253–265.
- 1056 Somasundaran, P. (2006). *Encyclopedia of surface and colloid science* (Vol. 2). CRC
1057 press, New York, London.
- 1058 Stebner, H., & Hördt, A. (2017). Simulation of membrane polarization of porous me-
1059 dia with impedance networks. *submitted to Near Surface Geophysics*.
- 1060 Titov, K., Kemna, A., Tarasov, A., & Vereecken, H. (2004). Induced polarization
1061 of unsaturated sands determined through time domain measurements. *Vadose*
1062 *Zone Journal*, 3(4), 1160-1168.
- 1063 Titov, K., Komarov, V., Tarasov, V., & Levitski, A. (2002). Theoretical and exper-
1064 imental study of time domain-induced polarization in water-saturated sands.
1065 *Journal of Applied Geophysics*, 50(4), 417 - 433.
- 1066 Volkmann, J., & Klitzsch, N. (2010). Frequency-dependent electric properties of
1067 microscale rock models for frequencies from one millihertz to ten kilohertz. *Va-*
1068 *dose Zone Journal*, 9(4), 858-870.
- 1069 Wagner, K. W. (1914). Erklärung der Dielektrischen Nachwirkungsvorgänge auf
1070 Grund Maxwellscher Vorstellungen. *Electrical Engineering (Archiv fur Elek-*
1071 *trotechnik)*, 2(9), 371–387.
- 1072 Wainwright, H. M., Flores Orozco, A., Bucker, M., Dafflon, B., Chen, J., Hubbard,

1073
1074
1075
1076
1077
1078

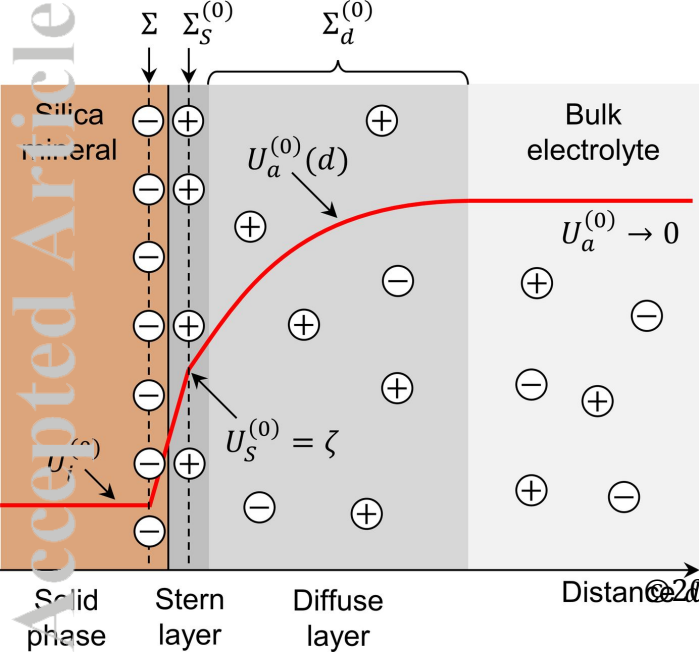
S. S., & Williams, K. H. (2015). Hierarchical bayesian method for mapping biogeochemical hot spots using induced polarization imaging. *Water Resources Research*.

Zukoski, C., & Saville, D. (1986). The interpretation of electrokinetic measurements using a dynamic model of the Stern layer: II. Comparisons between theory and experiment. *Journal of colloid and interface science*, *114*(1), 45–53.

Accepted Article

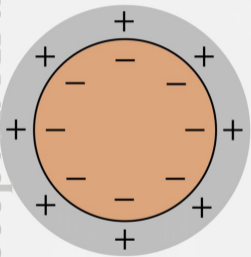
Figure 1.

Accepted Article

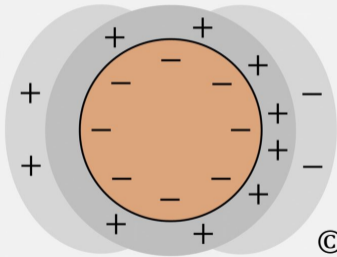


Accepted Article

(a)

 $\mathbf{E} = 0$ 

(b)

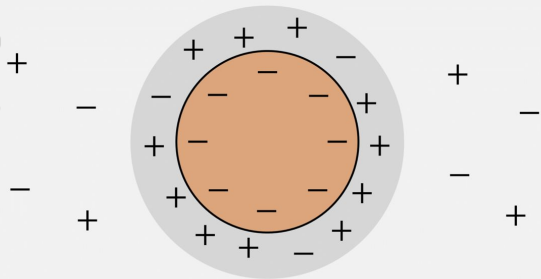
 $\mathbf{E} \rightarrow$ 

©20

Figure 3.

Accepted Article

(a)

 $\mathbf{E} = 0$ 

(b)

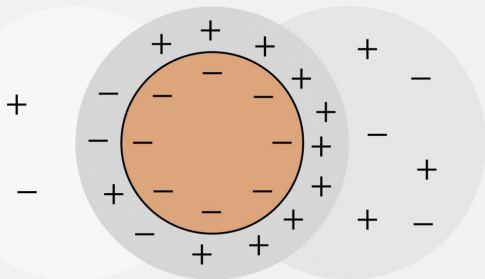
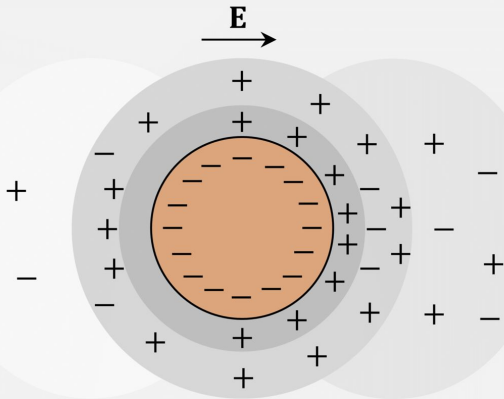
 $\mathbf{E} \rightarrow$ 

Figure 4.

Accepted Article



Accepted Article

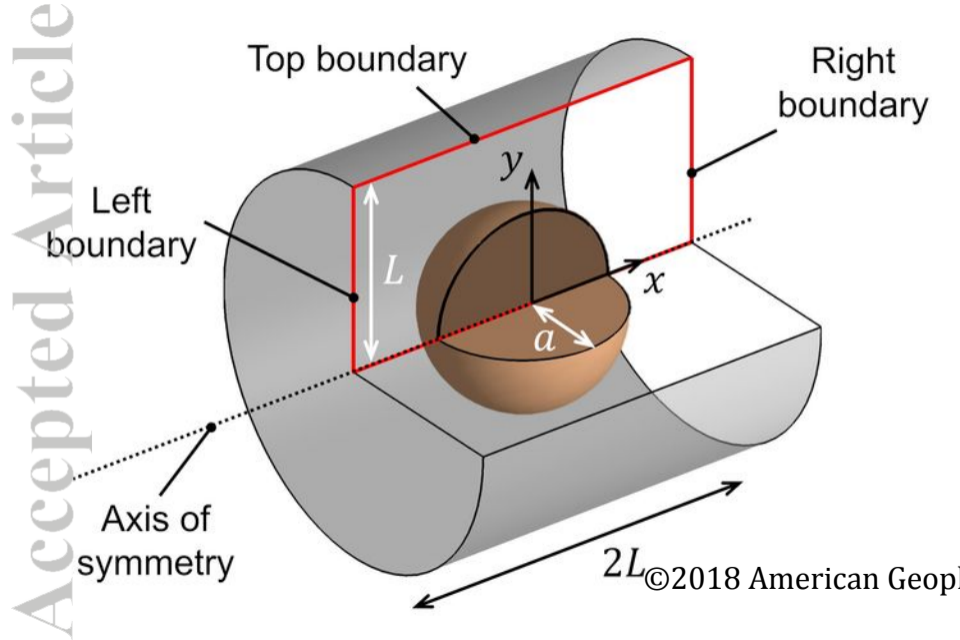
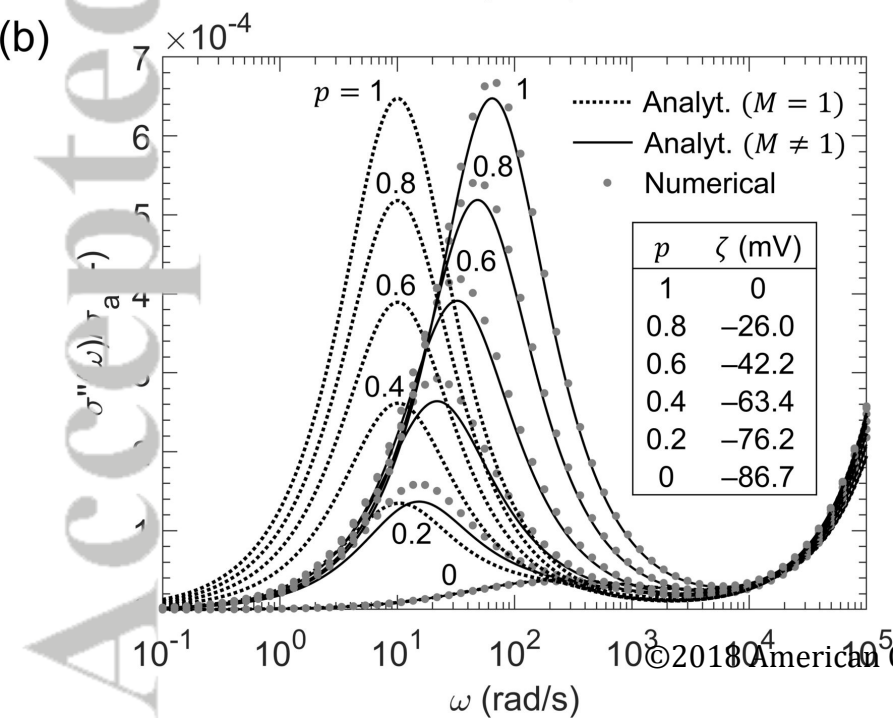
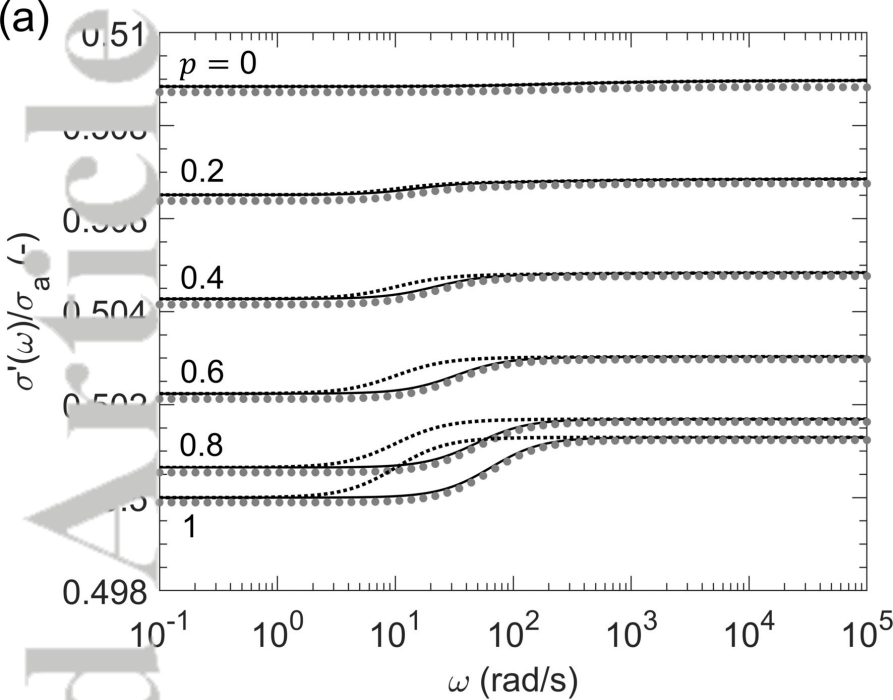
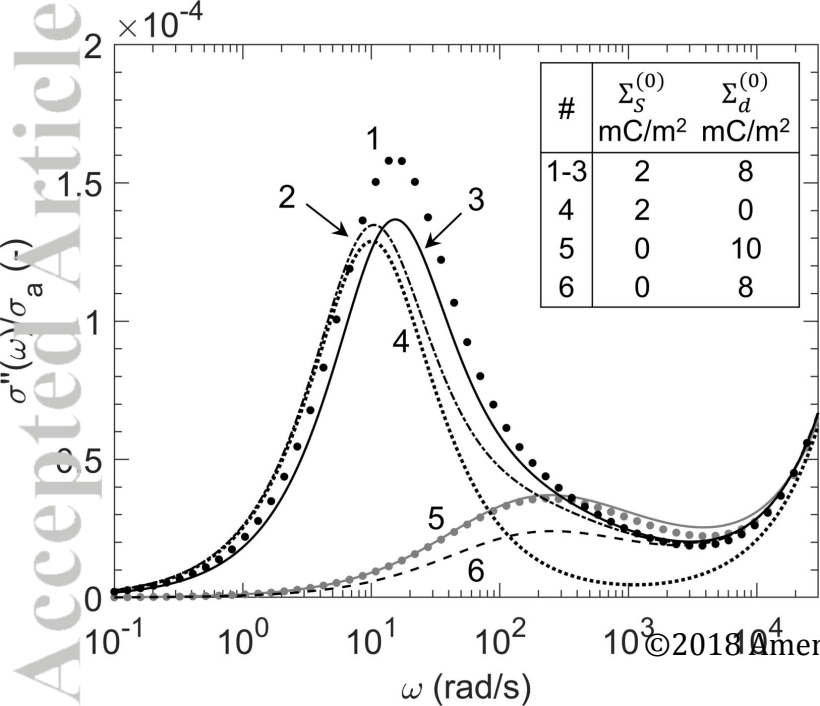


Figure 6.

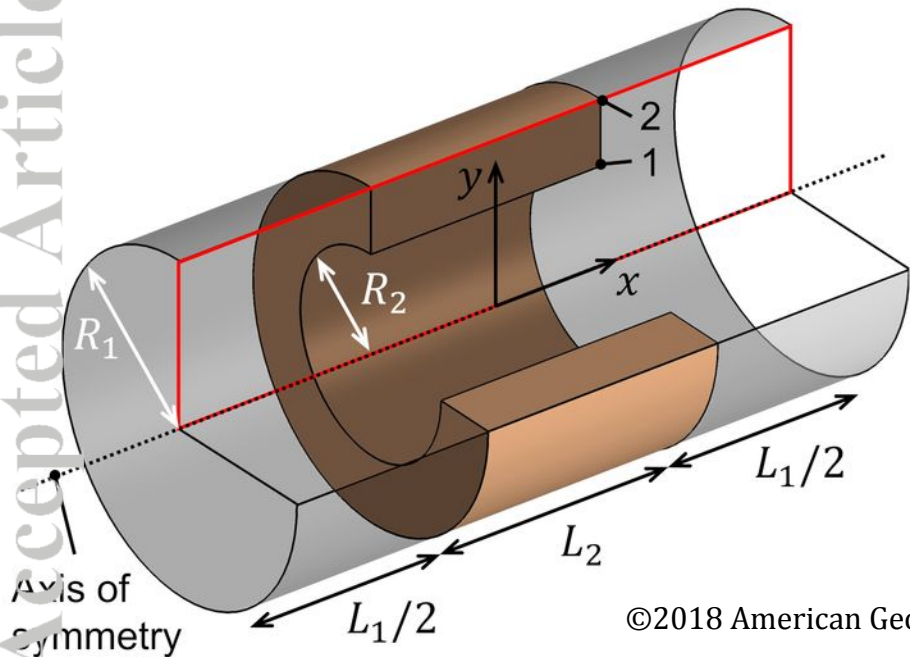
Accepted Article



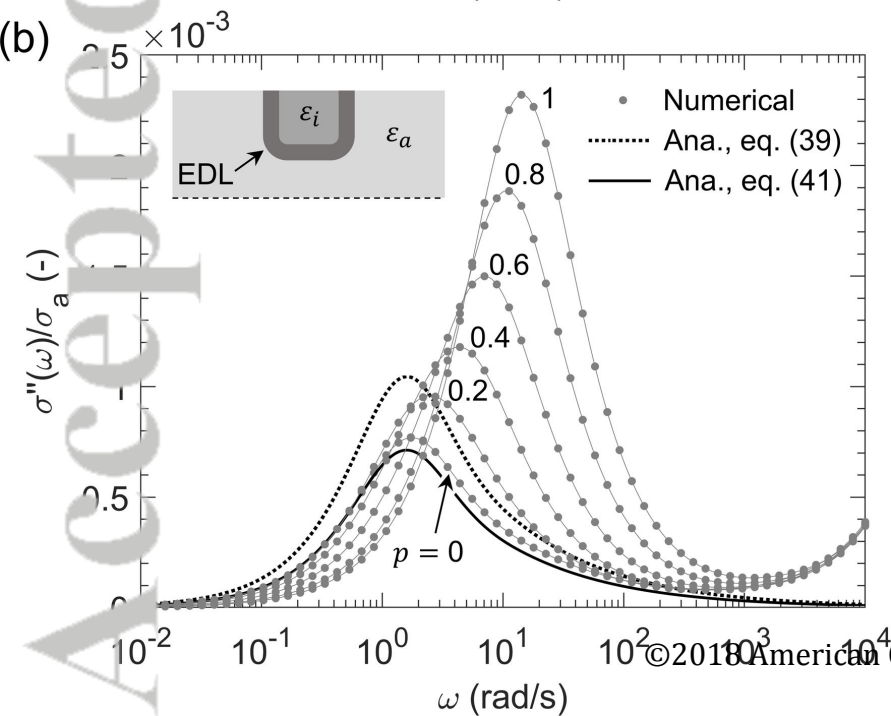
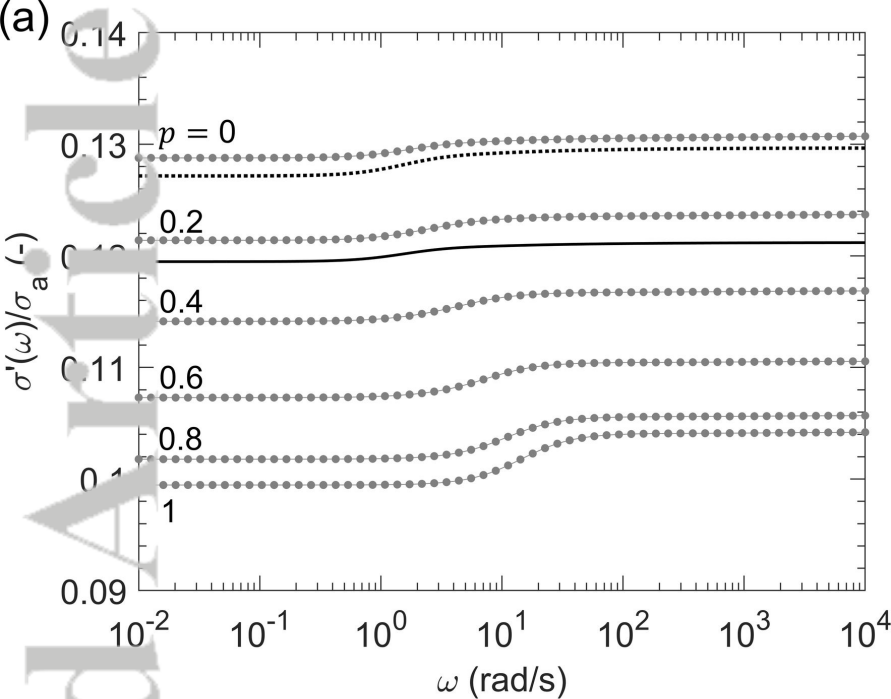
Accepted Article



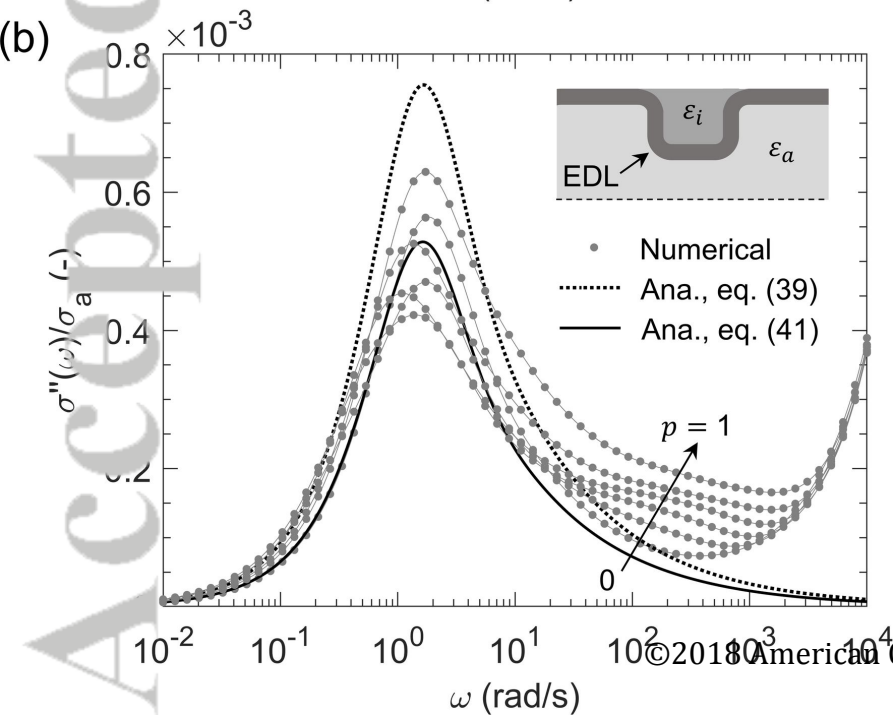
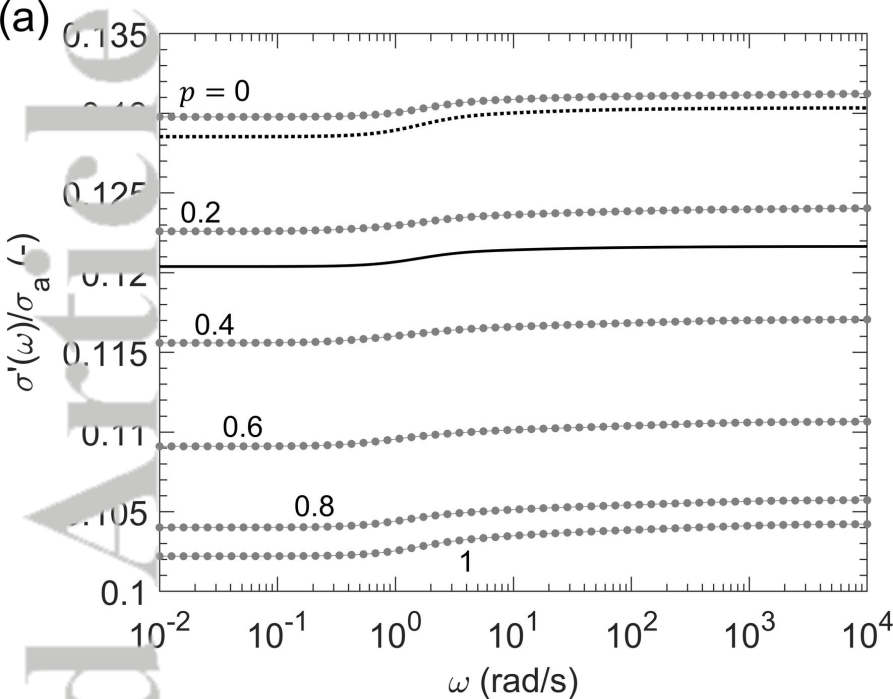
Accepted Article

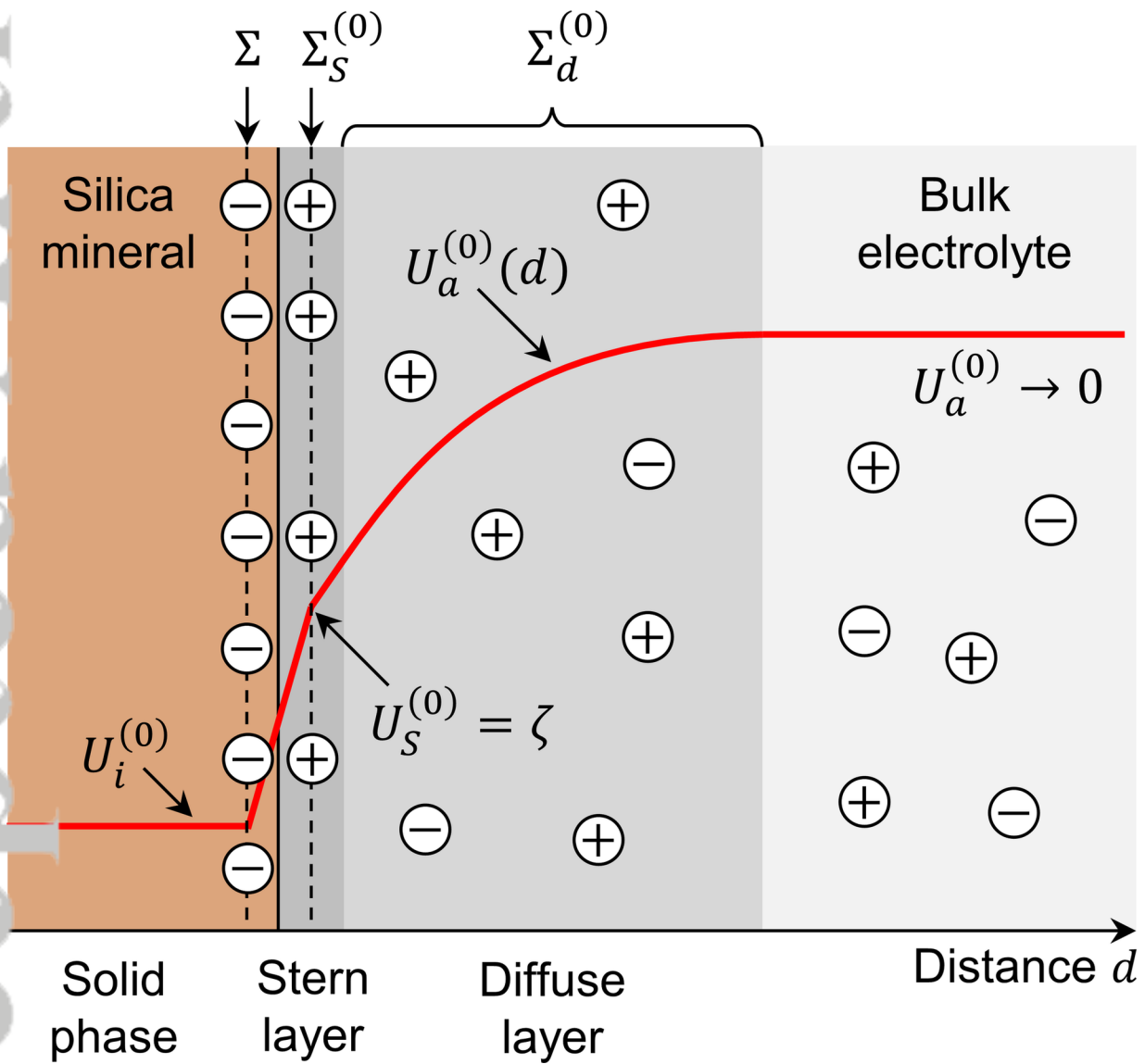


Accepted Article

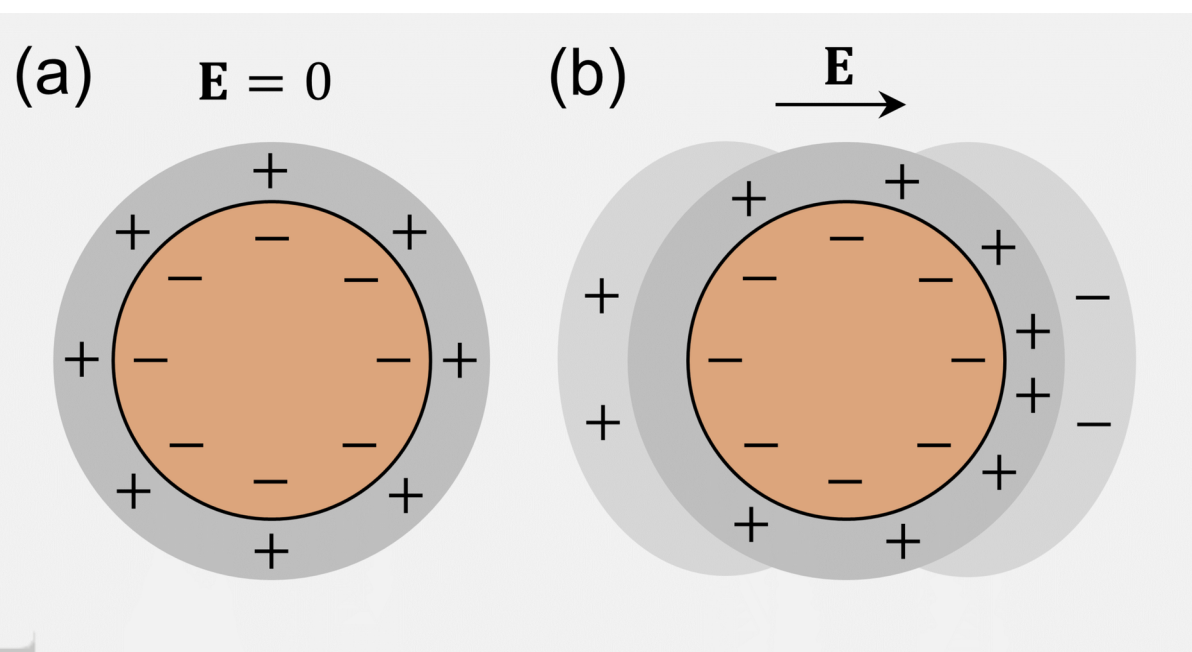


Accepted Article

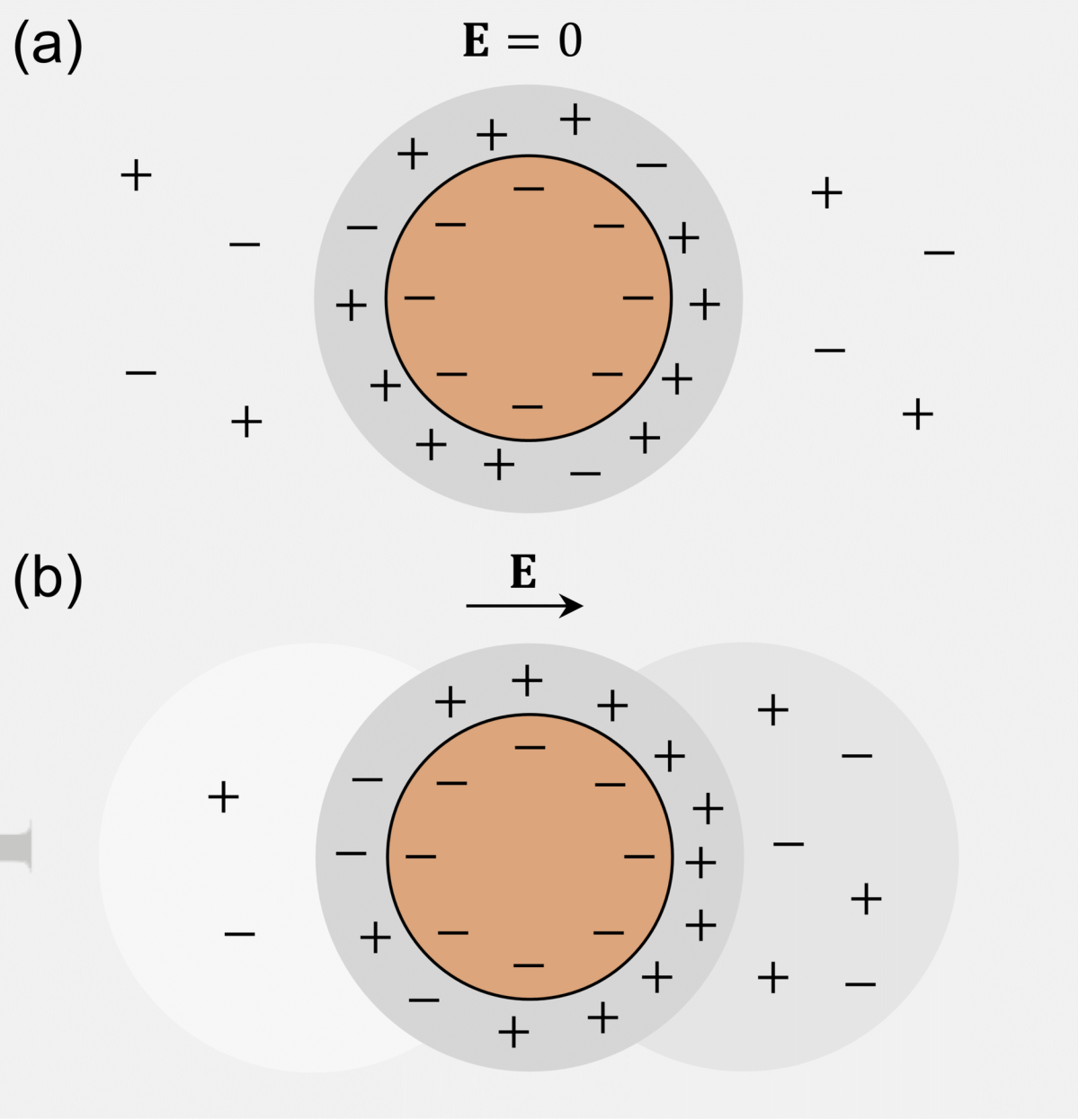




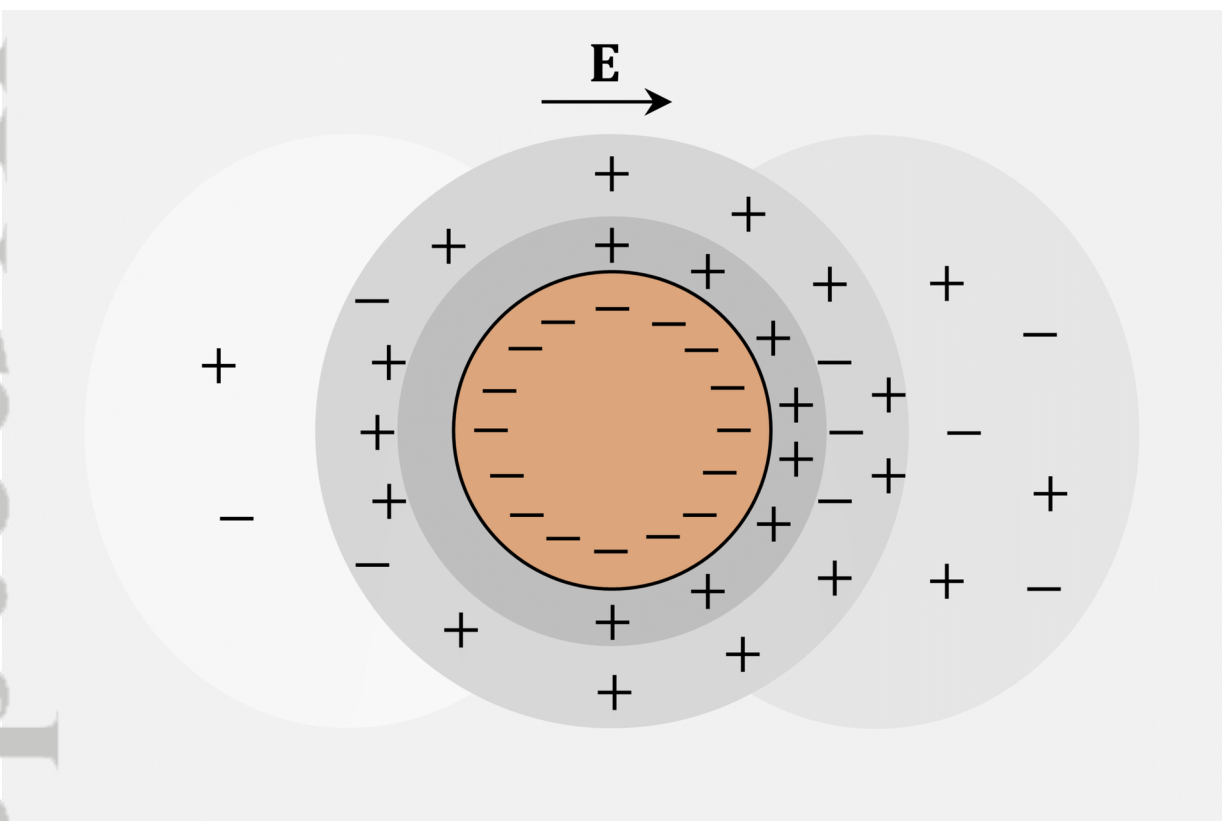
2019JB017679-f01-z.png



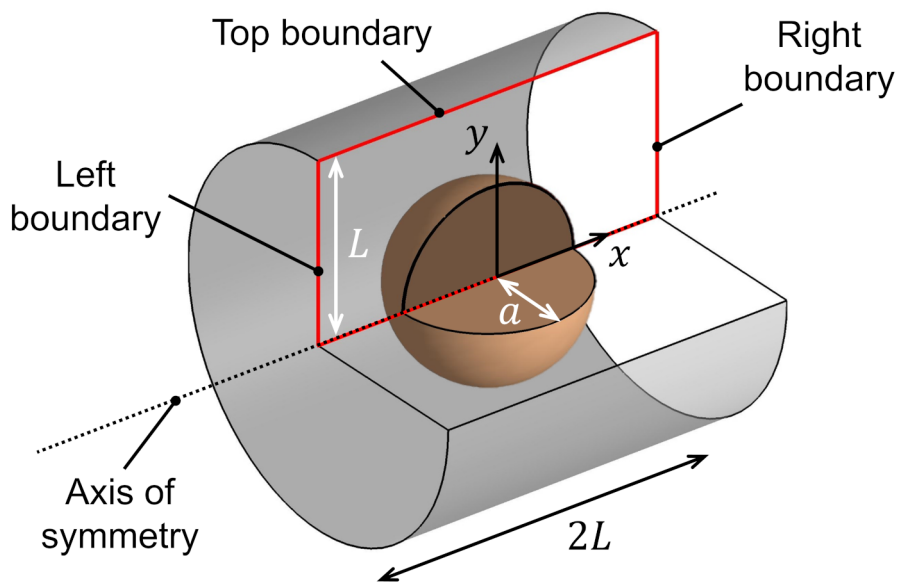
2019JB017679-f02-z-.png



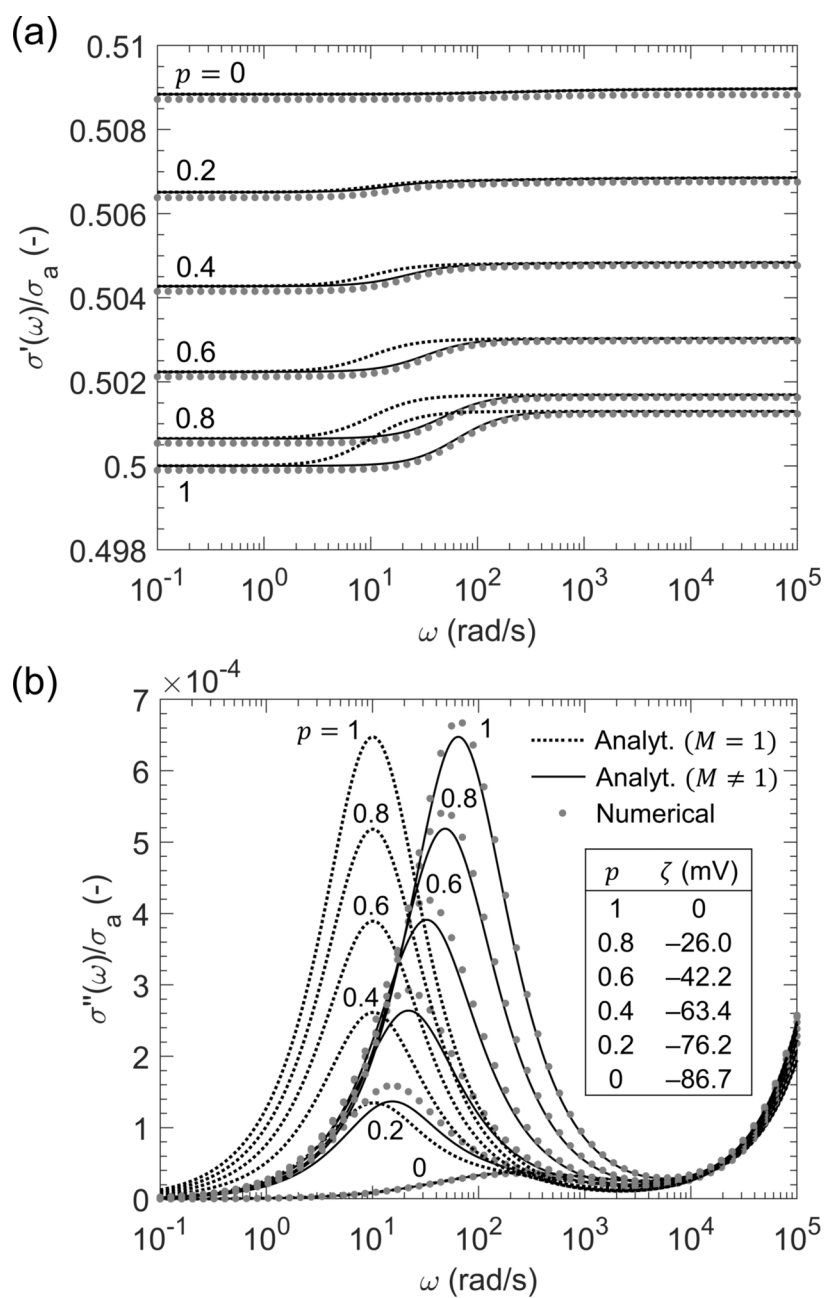
2019JB017679-f03-z.png



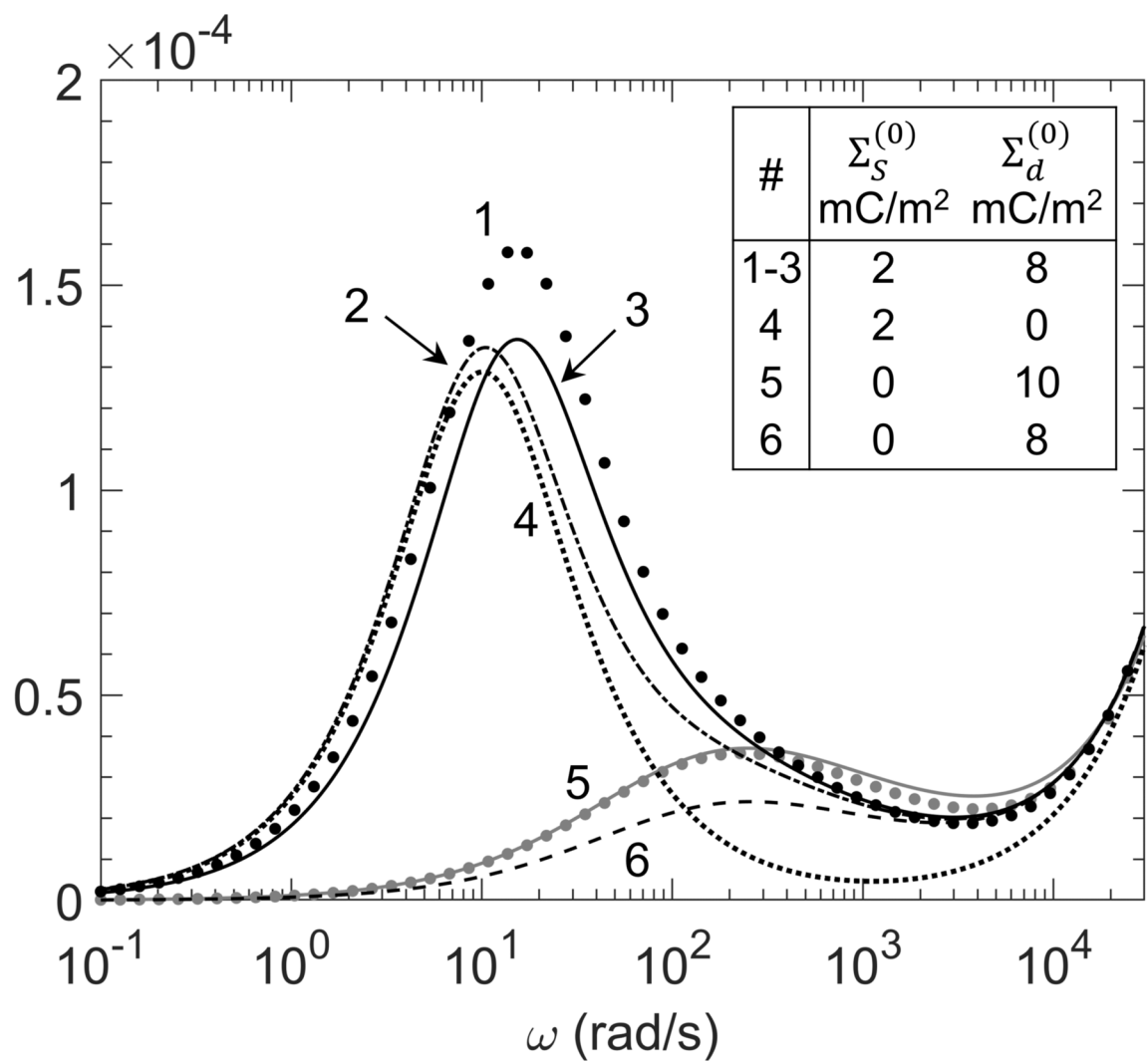
2019JB017679-f04-z-.png



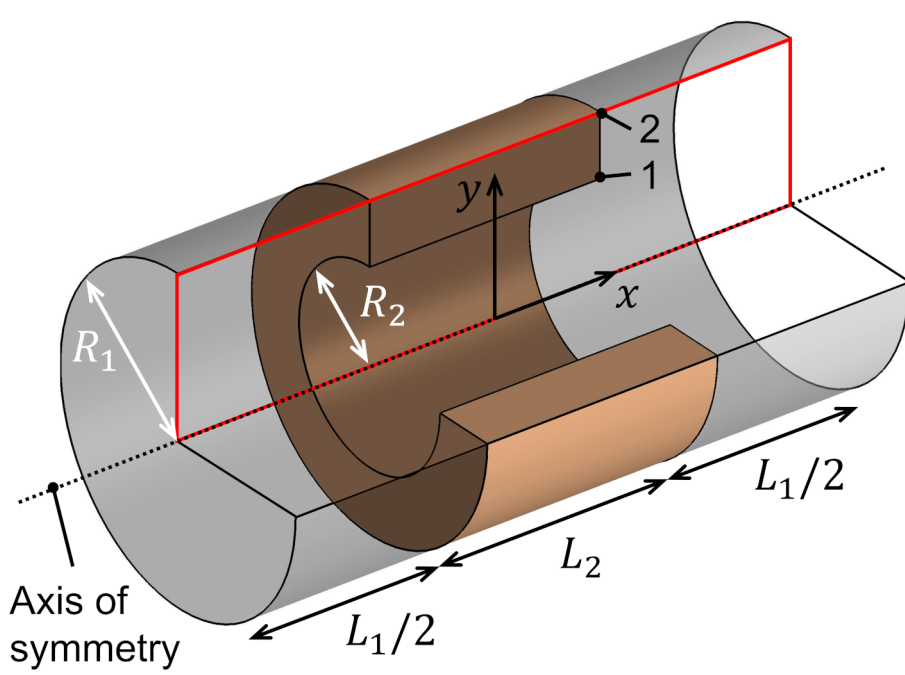
2019JB017679-f05-z-.png



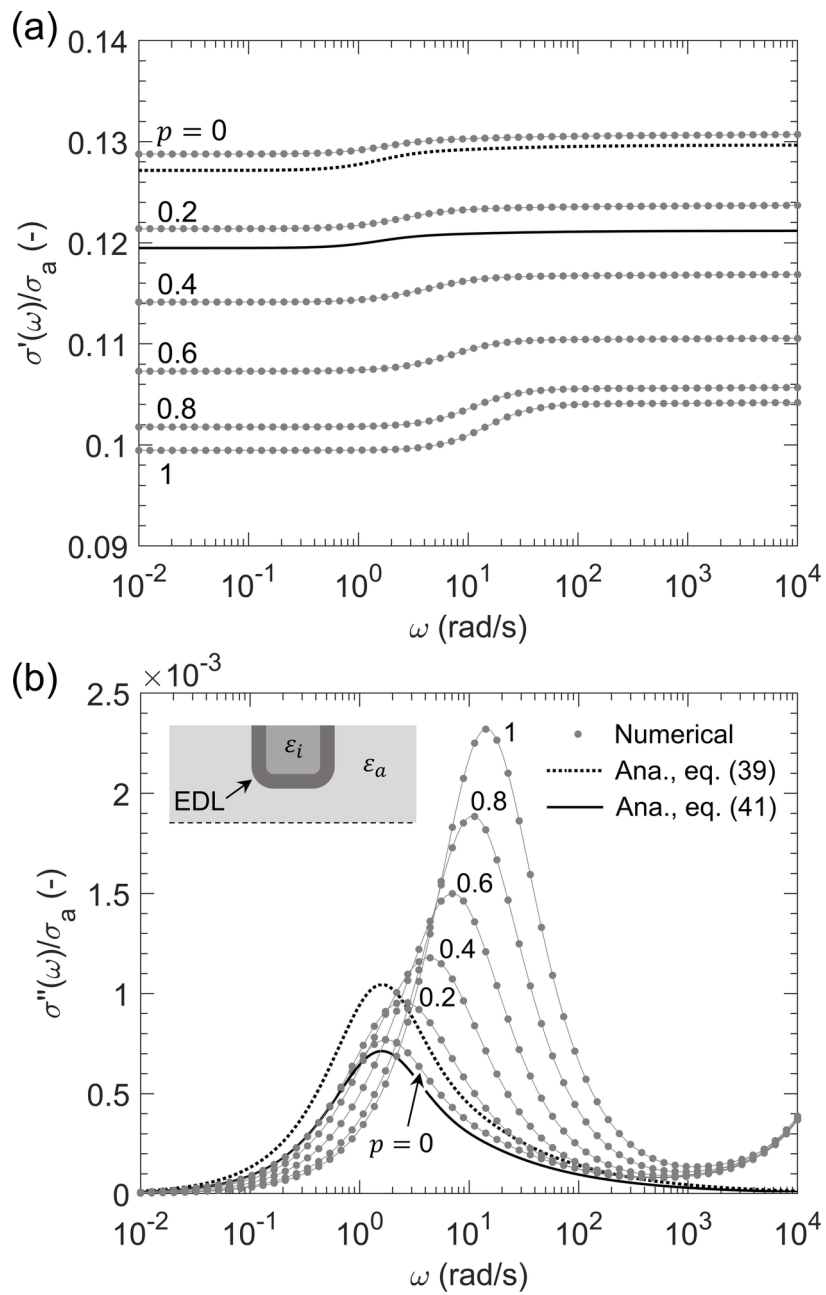
2019JB017679-f06-z-.png



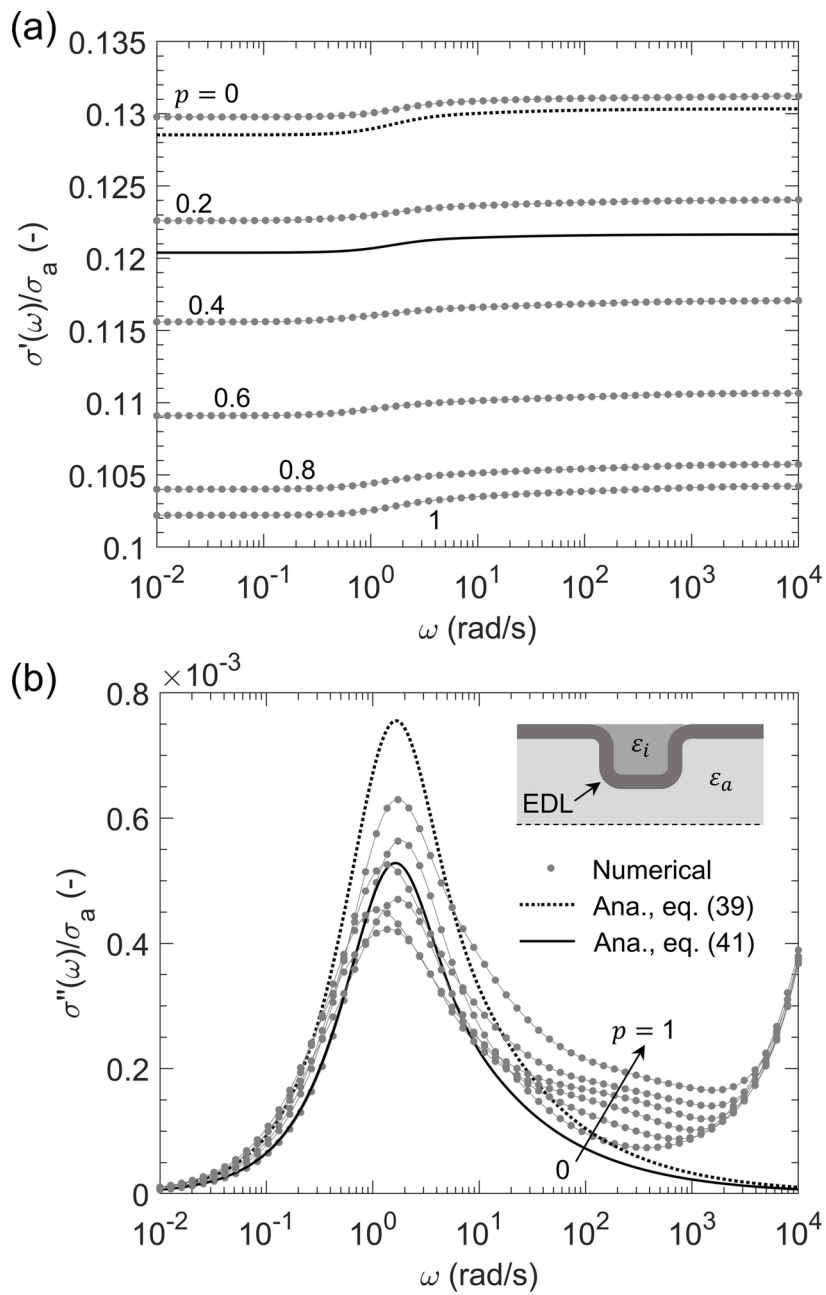
2019JB017679-f07-z-.png



2019JB017679-f08-z.png



2019JB017679-f09-z-.png



2019JB017679-f10-z.png